UCLouvain

École polytechnique de Louvain

Landing trajectories analysis and geophysics of Juventas in the binary asteroid system Didymos

Author: Guillaume Roisin
Supervisors: **Philippe Chatelain, Veronique Dehant**
Readers: **Pierre Schrooyen, Ozgur Karatekin**

Academic year 2021–2022
Master [120] in Mathematical Engineering

Abstract

On February 15, 2013, a 20m meteor exploded over Chelyabinsk, Russia, generating a flash brighter than the sun and creating a shockwave injuring 1,500 people. The blast was so strong that it yielded 26 to 33 times as much energy as the Hiroshima atomic bomb. This incident was a reminder of the importance of monitoring near-Earth objects and having planetary defense systems. Astronomers have estimated that there are tens of thousands of near-Earth objects of more than 140 meters that could cause regional devastation if they hit Earth. In this context, the Asteroid Impact and Deflection Assessment (AIDA) mission jointly led by NASA and ESA is part of humanity's planetary defense mission to attempt the first ever deflection of a celestial body in the solar system. The Double Asteroid Redirection Test (DART) spacecraft developed by NASA and the Johns Hopkins Applied Physics Laboratory will slam into the moon of the binary asteroid 65803 Didymos to shift its orbit. Five years later the Hera spacecraft developed by ESA will study the impact caused by DART and one of Hera's additional landers, the Juventas CubeSat, will attempt to land on the asteroid. This thesis focuses on the landing phase of the Juventas CubeSat to study a set of reliable landing trajectories. The dynamical environment of the CubeSat in the Didymos system and the landing phase are first presented. A numerical integrator to efficiently compute landing trajectories is proposed and studied. A braking maneuver during the descent is implemented and shape models are added to represent the asteroid. The interaction with the surface of the asteroid is also modeled. Finally, a Monte Carlo analysis to study the robustness of the found landing trajectory is performed.

Acknowledgments

I would first like to thank Prof. Veronique Dehant and Prof. Philippe Chatelain for allowing me to keep working on such an interesting project. Being in applied mathematics and having completed a minor in physics, this thesis is a great opportunity to combine my passion for astronomy with the knowledge I have acquired during my studies.

Thank you to Guillaume Vanhalst and Guillaume Hanon who produced the thesis that I based my work on. I had the opportunity to continue their work, especially thanks to my best friend Guillaume Vanhalst, who answered my (many) questions during the year.

I would also like to say a huge thank you to Ozgur Karatekin who supervised my thesis every week for a year. His help and patience were invaluable.

At the Royal Observatory of Belgium, I would first like to thank Guillaume Noiset for helping me these last few months and especially in reviewing my thesis and giving me advice. I would also like to thank Gregoire Henry and Elisa Tasev for their help, as well as Alfonso Calderio. But also a particular acknowledgment to Bart Van Hove for his challenging insights and precious help.

Finally, I would also especially like to thank Victor Manuel Moreno Villa, Carlos Sánchez Lara and Giovanni Bay at GMV who worked with me on the second part of my thesis by providing me with valuable resources. Thank you for taking the time to answer my questions and to guide me through the completion of my thesis.

Contents

Introduction

On November 24, 2021, many members of the general public heard for the first time about NASA's first planetary defense mission: the Double Asteroid Redirection Test (DART) mission. Using a Falcon 9 rocket, DART took off from Vandenberg base in California and embarked on a 9-month journey to the moon of the binary asteroid system 65803 Didymos. DART will impact the asteroid to try to deviate its orbit. This will be humanity's first ever attempt at deflecting a celestial object. Five years later, ESA will send the Hera spacecraft to analyze the dynamical environment of Didymos and study the crater formed by DART's impact.

Hera will also launch two CubeSats Milani and Juventas to obtain additional data on the asteroid. Juventas is being developed by two private companies GomSpace and GMV jointly with the Royal Observatory of Belgium (ROB) and other space agencies in Europe. This thesis is part of the project work for the ROB to study the landing phase and geophysics of Juventas.

This thesis extends the work of Vanhalst and Hanon (2020) [14] who studied the landing phase of Juventas in their thesis : *A study of the landing phase of the Juventas CubeSat on the moon of the binary asteroid system Didymos.* In their work, a numerical tool to model Juventas in the vicinity of Didymos was first designed and built in Matlab. Then, the study of direct landing strategies was proposed to find a set of reliable landing trajectories. These trajectories and the bouncing model developed were studied through a Monte Carlo analysis to take into account the uncertainties relative to the model and find optimal landing trajectories.

Thesis structure

Studying and finding optimal landing trajectories is time-consuming as tens of thousands of trajectories are computed. It is of great interest for the ROB to build a reliable numerical tool able to compute many trajectories efficiently and rapidly for further similar projects. In this context, an optimized vectorized numerical integrator is proposed and compared with the performance of the code developed by Vahalst and Hanon (2020). Then, the numerical model developed by Vanhalst and Hanon (2020) is improved to take into consideration more realistic features. A braking maneuver is added at the end of the trajectory. Dimorphos is modeled by shape models to represent any arbitrary shape of the asteroid. The interaction with the surface of the different models of Dimorphos is considered. Finally, a Monte Carlo analysis of the nominal trajectory will be performed to assess the robustness of the found trajectory.

Chapter 1 presents and gives context for the mission related to this thesis. The AIDA collaboration and its two missions (DART and Hera) are introduced. The Didymos system and its physical and dynamical parameters are presented. Then, the Juventas CubeSat configuration, science objectives and mission phases are presented.

Chapter 2 is dedicated to the modelization of Juventas in the Didymos system. The equations of motion are derived and orbital perturbation are added to the model. Finally, the numerical integrator is proposed to solve the equations.

Chapter 3 proposes a review of the landing phase analysis studied in the thesis of Vanhalst and Hanon (2020). The landing phase analysis is composed of the landing strategy through a backward propagation and then the analysis of the uncertainties through a Monte Carlo analysis.

Chapter 4 proposes an optimization of the code written by Vanhalst and Hanon (2020) to compute propagated trajectories through vectorization. A variable step Runge-Kutta Fehlberg integrator is proposed and validated. Then, the implementation of a vectorized version of the integrator is studied. Finally, the performance of the vectorized integrator is discussed.

Chapter 5 is dedicated to the study of the nominal trajectory proposed by GMV. First a new orbital perturbation is added to the model and validated. Then the implementation of a braking maneuver at the end of trajectory is studied. To make the model more realistic, shape models are introduced. The implementation of the interaction with the surface through a bouncing model is presented and implemented to work on shape models too.

Chapter 6 provides an analysis of the uncertainties related to the nominal trajectory to study its robustness through a Monte Carlo analysis. The landing and bouncing are discussed for different scenarios.

Finally, a conclusion will be proposed highlighting the main contributions of this thesis and presenting future suggested researches.

Chapter 1

Mission Description

This chapter provides some context for the ongoing mission related to this thesis. First, the AIDA mission is introduced and its two independent missions : DART and Hera are presented. The Didymos system is introduced next, as well as its physical and dynamical parameters. The Juventas CubeSat is then described, along with its science objectives and its mission phases.

1.1 AIDA mission

The Asteroid Impact and Deflection Assessment (AIDA) mission is a joint collaboration between NASA and ESA to perform the first demonstration of the deflection of a small near-Earth asteroid by kinetic impact. The target of the AIDA mission is the binary asteroid system 65803 Didymos [22].

AIDA consists of two independent but complementary missions : the DART mission led by NASA will impact the asteroid and the Hera mission led by ESA will later study and observe the impact.

1.1.1 DART

The Double Asteroid Redirection Test (DART) will impact the moon of the Didymos system at a speed of approximately 6.6 km/s to try to deviate its orbit. The DART spacecraft was built by the Johns Hopkins Applied Physics Laboratory (APL).

The DART spacecraft also carries the LICIACube 6U CubeSat developed by the Italian Space Agency. The LICIACube will be released 10 days before impact and is built to make observations and provide images of the Didymos system after impact [16].

The DART spacecraft was launched on 24 November 2021 on a SpaceX Falcon 9 rocket at 06:21:02 UTC. DART's collision with Dimorphos is planned to occur on 26 September 2022 [23].

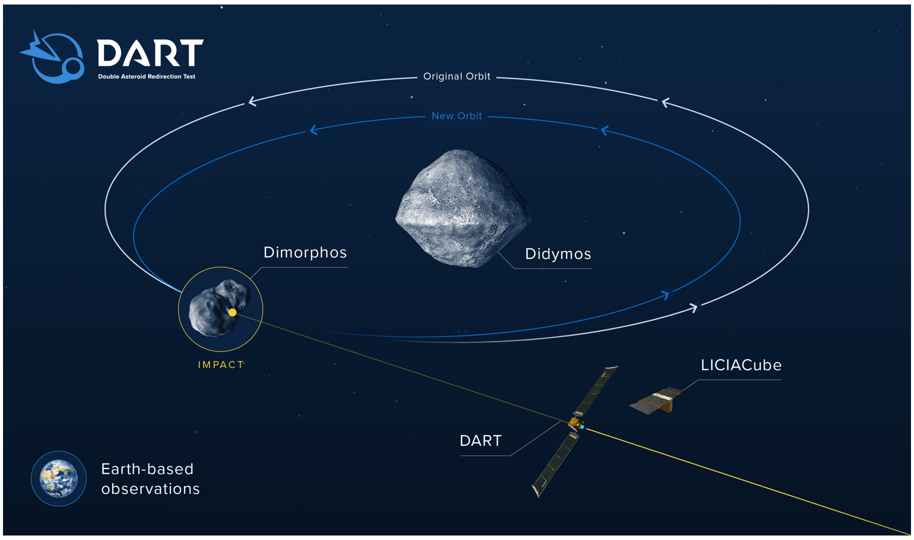

Figure 1.1: DART infographic [23].

1.1.2 Hera

The Hera spacecraft is being developed by ESA's space safety program, its launch is slated for 2024 and it should reach the Didymos system in 2027, five years after DART's impact. Hera will perform at least 6 months of measurements to understand the effect of DART's impact on the smaller body of the Didymos system, in particular measuring its internal properties such as its mass and the characterization of the crater [3].

Hera's payload is composed of asteroid framing cameras, a planetary altimeter, a thermal infrared imager and two 6U CubeSats Juventas and Milani [3]. After approximately two months of observations, Hera will release the two CubeSats each equipped with their own payload to obtain additional data on the asteroid.

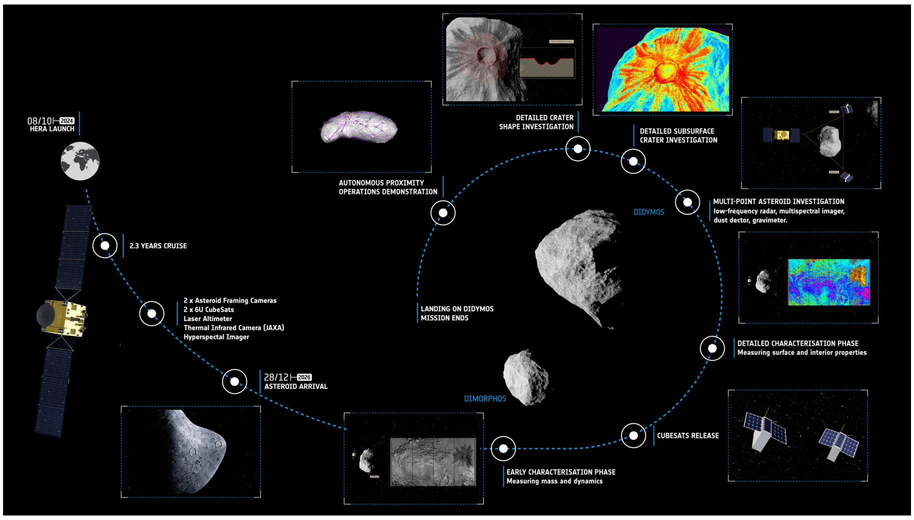

Figure 1.2: Hera infographic [31].

1.2 Didymos system

The binary asteroid system considered in this study is the binary asteroid 65803 Didymos. It is composed of the main body called Didymos and the second body orbiting around it is called Dimorphos. Near-Earth asteroid Didymos was discovered in 1996 and has a heliocentric semi-major axis of 1.644 AU. In 2003, Dimorphos was discovered and Didymos turned out to be a binary system.

Didymos and Dimorphos shape models are shown in Figure 1.3 thanks to photometric light curve and radar data. Dimorphos is considered as an ellipsoid model. The bulk density of Dimorphos is assumed to be the same as Didymos.

The physical and dynamical parameters of the Didymos system is presented in Table 1.1. These parameters are currently the nominal parameters used by the teams working on the mission but will be updated when new measurements become available.

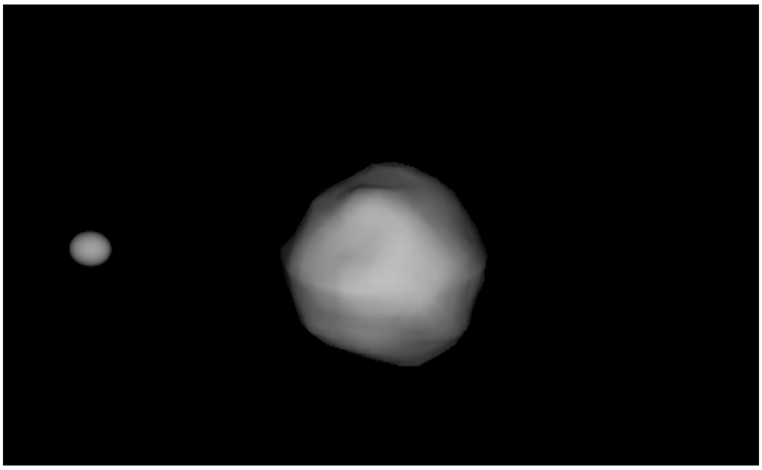

Figure 1.3: Shape model of Didymos and Dimorphos, based on photometric light curve and radar data [2].

Parameters	**Value**	**Units**
Semi major axis	1.19 ± 0.03	km
Diameter of Didymos	780 ± 30	m
Diameter of Dimorphos	164 ± 18	m
Diameter ratio	0.21 ± 0.01	-
Didymos principal axis x, y, z	832 ± 3%, 837 ± 3%, 786 ± 5%;	m
Dimorphos principal axis x, y, z	208, 160, 133	m
Dimorphos orbital period	11.921626 ± 0.000018	h
Dimorphos orbital eccentricity e	0.03	-
Total mass of the system	$5.278e^{11} \pm 0.54e^{11}$	kg
Didymos bulk density	2170 ± 350	kg m^{-3}
Dimorphos bulk density	2170 ± 350	kg m^{-3}
Rotation period of Didymos	2.2600 ± 0.0001	h
Heliocentric eccentricity	$0.383752501 \pm 7.7e^{-9}$	h
Heliocentric semimajor axis	$1.6444327821 \pm 9.8e^{-9}$	AU
Heliocentric inclination to the ecliptic	$3.4076499 \pm 2.4e^{-6}$	$\circ$

Table 1.1: Physical and dynamical paramaters of the Didymos system [1].

1.3 Juventas CubeSat

Juventas is a 12kg 6U CubeSat located on the Hera mothercraft. The Juventas payload is composed of a Low-Frequency Radar (LFR), a 3-axis gravimeter, an accelerometer, a visible camera and an Inter-Satellite Link (ISL). The spacecraft includes the electronics for the Guidance, Navigation and Control (GNC). Juventas is composed of a cold-gas propulsion system [12] and lithium ion cell batteries [30]. Attitude determination is done through the star tracker, sun sensors and gyros. The composition of the Juventas CubeSat is presented in Figure 1.4a.

Juventas has two deployable solar arrays that can generate up to 35 W at 1.8 AU. and antennas with 1.36m deployed length (this configuration is shown in Figure 1.4b).

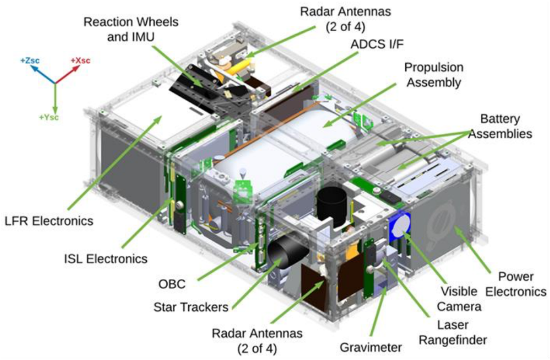

(a) Schematic structure of Juventas [15].

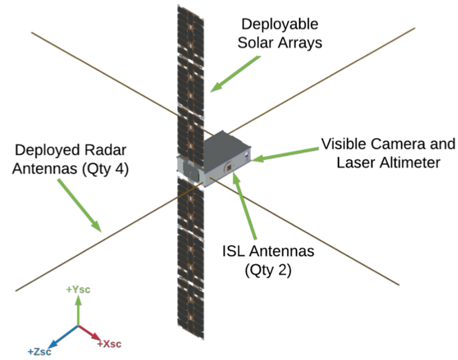

(b) Juventas in deployed configuration [17].

Figure 1.4: Juventas CubeSat.

1.3.1 Science objectives

The Juventas CubeSat is complementary to the Hera mission as it will contribute to the study of the binary asteroids as well as understanding their formation processes, their internal structure, their dynamical environment and their surface composition. This will be done through the following 5 Science objectives [17]:

- Science Objective 1: Characterize the gravity field of Dimorphos
- Science Objective 2: Characterize the internal structure of Dimorphos
- Science Objective 3: Characterize the surface properties of Dimorphos
- Secondary Science Objective 4: Determine the dynamical properties of Dimorphos

- Secondary Science Objective 5: Characterize the surface and subsurface properties of Didymos

1.3.2 Mission phases

The operations of the Juventas CubeSat are divided into 5 mission phases [15]:

- Launch and commissioning phase (CP) : Duration of 7 + 3 days [1]
- Transfer into observations phase (TP) : Duration of 1 day
- Global observations phase (GOP) : Duration of 30 days
- Proximity observations phase (POP) : Duration of 30 days
- Landing phase (LP) : Duration of 1 day

Launch and commissioning phase (CP)

This phase is composed of a single arc of seven days and up to 4 additional arcs are possible for a total of 21 days. The Juventas spacecraft will be released from Hera mothercraft with a low velocity in one of these arcs. Juventas has to be inserted in a safe trajectory with a minimum of four days without operations. A maximum distance of 50km with Hera must be respected to ensure the communication between the two spacecraft (maximum ISL range).

Transfer into observations phases (TP)

After the CP, Juventas will be injected into a Self-Stabilized Terminator Orbit (SSTO). SSTOs are chosen for the observations phases where the surface characterization of the Didymos system will be performed.

The SSTO orbit is characterized along the Sun-terminator of Didymos and quasi perpendicular to the plane between Dimorphos and the ecliptic. This orbit is chosen for its stability as well as to minimize the required deltaV to maintain the orbit [30].

During the observations phases, Juventas will stay in the SSTO and perform its primary objectives with the Low-Frequency Radar (LFR) and radio science measurements with the Inter-Satellite Link (ISL) radio to the Hera spacecraft [30]. More than 70% of coverage of Didymos and Dimorphos can be expected during the 60 days of observations [15].

[1] can be extended to a maximum of 14 days

The 3.3km and 2km SSTOs are considered for the observations phases and can be seen in Figure 1.5.

Global observations phase (GOP)

The Juventas CubeSat will be inserted in a 3.3 km SSTO.

Proximity observations phase (POP)

For the proximity observations phase, the spacecraft will be inserted in a 2 km SSTO.

Landing phase (LP)

After the POP, Juventas will leave the 2 km SSTO and try to land on Dimorphos with a relative impact velocity less or equal to 10 cm/s. A direct landing strategy is considered where one deltaV maneuver is performed while leaving the SSTO. A second deltaV maneuver (braking maneuver) could be performed close to the surface of Dimorphos to reduce the impact velocity [15].

During the descent, the on-board camera will take images of Dimorphos and if possible of the DART impact site. With these images, a better understanding of the surface properties of Dimorphos will be possible.

During the impact and before coming to rest, Juventas will use its 3-axis gravimeter, accelerometer and gyros to study the dynamics of the impact with the surface of Dimorphos and will be able to reconstruct the coefficient of restitution of the surface to study the regolith material.

After landing and if the spacecraft is still operational, Juventas will be able to perform its final science objectives to study the local gravitational field and the dynamical properties of Dimorphos [30].

The description of the Juventas Science objectives and mission phases as well as the equipment used is summarized in Table 1.2.

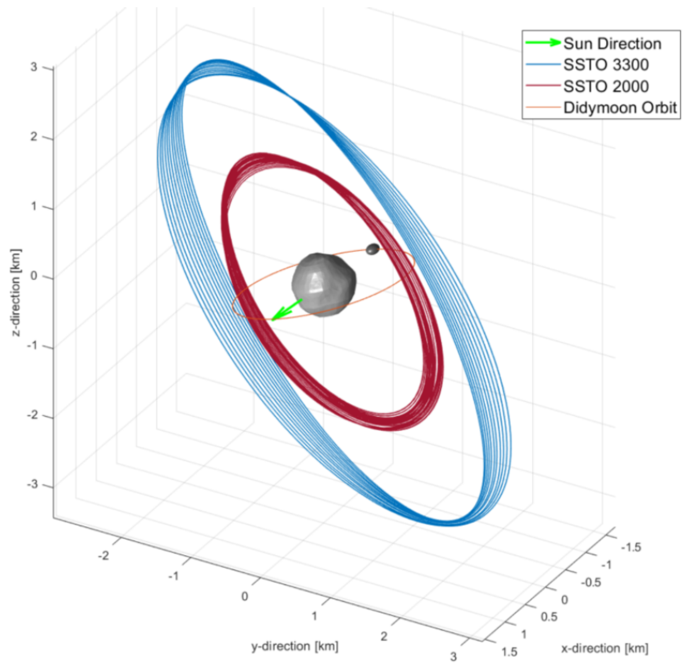

Figure 1.5: 3.3 km and 2 km SSTOs for 30-day coverage.

Science Objective	Investigation	Measurements	Instruments	Mission Phase
Gravity field of Didymoon	Gravity field characterisation outside Brillouin sphere at least up to degree & order 2	Deflection during orbit measured with ranging, LoS to HERA (second CubeSat)	ISL radio link	Proximity operations
	Surface gravity	Surface acceleration	Gravimeter	Surface operations
	CubeSat descent/touch-down/bouncing	Dynamic recording of each event	GNC	Landing/Bouncing
Internal structure of Didymoon	Reconstruction of material density & largest monolithic object	Properties of (back-)reflection of transmitted signal	Low frequency radar	Proximity operations
Gravity field of Didymoon	Visible imaging	Inspection of Didymoon surface features and impact crater	Visible camera	Proximity operations, Surface operations
	Surface strength measurement	Rebounds from the surface	IMU	Landing/Bouncing
Dynamical properties of Didymoon	Orbital analysis	Orbital analysis by ranging LoS to HERA (second CubeSat)	ISL radio link	Surface operations
	Variable surface acceleration	Surface acceleration measurements over >1 orbit	Gravimeter	Surface operations
	Attitude and Time dependent surface illumination	Attitude and time dependent surface illumination	Star tracker, sun sensors	Surface operations
Surface/sub-Surface properties of Didymos	Reconstruction of material density & largest monolithic object	Properties of (back-)reflection of transmitted signal	Low frequency radar	Proximity operations

Table 1.2: Juventas Science Objectives and Mission Phases, from [17].

Chapter 2

Model description

In this chapter, the Circular Restricted Three-Body Problem is presented and the equations of motion of Juventas in the Didymos system are derived. To make the model more realistic, orbital perturbations are added to form the Perturbed Circular-Restricted Three Body Problem. A quick overview of the numerical integration of this model will also be presented.

2.1 Circular Restricted Three-Body Problem

The model proposed by Vanhalst and Hanon (2020) to describe the motion of Juventas in the Didymos system is the Circular Restricted Three-Body Problem (CR3BP) and can be found in [25].

In the CR3BP, the two main bodies are considered massive compared to the third body. Thus the third body has no effect on the dynamics of the two main bodies [25]. In the Didymos system, the two main bodies are Didymos and Dimorphos and the third body is Juventas. Juventas has a mass of order 10^{-11} and 10^{-9} compared to the mass of Didymos and Dimorphos, respectively. The affect of Juventas on the two main bodies can be neglected. Thus, the CR3BP is a valid approximation to describe the motion of Juventas in the Didymos system. In this model, the bodies are modeled as point mass bodies.

The equations of motion in the CR3BP are defined in the rotating reference frame (also called synodic reference frame) $\mathcal{F} : \{\hat{\boldsymbol{e}}_r, \hat{\boldsymbol{e}}_\theta, \hat{\boldsymbol{e}}_3\}$. The origin of $\mathcal{F}$ is at the barycenter of the system, see Figure 2.1. The masses of Didymos, Dimorphos and Juventas are m_1, m_2 and m, respectively.

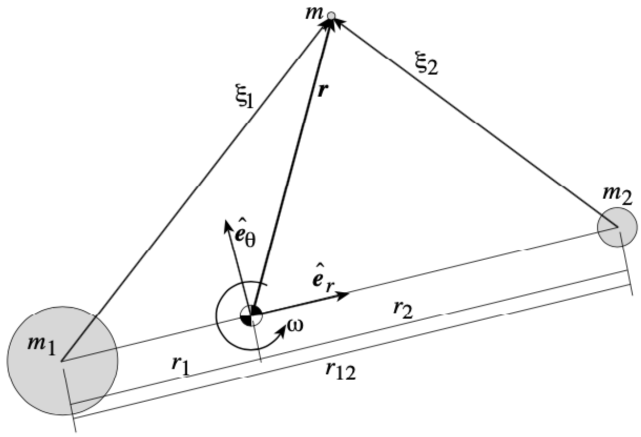

Figure 2.1: Illustration of the Circular Restricted Three-Body Problem from [25]

The frame $\mathcal{F}$ rotates with angular velocity $\boldsymbol{\omega} = \omega\hat{\boldsymbol{e}}_3$. In this frame the position vector $\boldsymbol{r}$ is expressed as

$$\boldsymbol{r} = r_x\hat{\boldsymbol{e}}_r + r_y\hat{\boldsymbol{e}}_\theta + r_z\hat{\boldsymbol{e}}_3 \tag{2.1}$$

The acceleration vector of r is given by

$$\ddot{\boldsymbol{r}} = (\ddot{r}_x - 2\dot{r}_y\omega - r_x\omega^2)\hat{\boldsymbol{e}}_r + (\ddot{r}_y + 2\dot{r}_x\omega - r_y\omega^2)\hat{\boldsymbol{e}}_\theta + \ddot{r}_z\hat{\boldsymbol{e}}_3 \tag{2.2}$$

The gravitational force $\boldsymbol{F}$ acting on Juventas by the two main bodies is expressed in frame $\mathcal{F}$ as

$$\boldsymbol{F} = -Gm\begin{bmatrix} \frac{m_1}{\xi_1^3}(r_x - r_1) + \frac{m_2}{\xi_2^3}(r_x - r_2) \\ (\frac{m_1}{\xi_1^3} + \frac{m_2}{\xi_2^3})r_y \\ (\frac{m_1}{\xi_1^3} + \frac{m_2}{\xi_2^3})r_z \end{bmatrix} \tag{2.3}$$

where ξ_i is given by

$$\xi_i = \sqrt{(r_x - r_i)^2 + r_y^2 + r_z^2} \tag{2.4}$$

Using Newton's second law,

$$\boldsymbol{F} = m\ddot{\boldsymbol{r}} \tag{2.5}$$

And thus substituting (2.2) and (2.3) into (2.5) yields the equations of motion of Juventas:

$$\begin{cases} \ddot{r}_x - 2\dot{r}_y\omega - r_x\omega^2 + G\Big(\frac{m_1}{\xi_1^3}(r_x - r_1) + \frac{m_2}{\xi_2^3}(r_x - r_2)\Big) &= 0 \\ \ddot{r}_y + 2\dot{r}_x\omega - r_y\omega^2 + G\Big(\frac{m_1}{\xi_1^3} + \frac{m_2}{\xi_2^3}\Big)r_y &= 0 \\ \ddot{r}_z + G\Big(\frac{m_1}{\xi_1^3} + \frac{m_2}{\xi_2^3}\Big)r_z &= 0 \end{cases} \tag{2.6}$$

From the CR3BP, some interesting quantities can be derived : the Jacobi integral and the Lagrange points. However, these two quantities are not addressed in this thesis because they are not needed in the analysis. If the reader is interested, more information can be found in Vanhalst and Hanon (2020).

2.2 Orbital perturbations

The CR3BP derived in section 2.1 is a simple model that considered Didymos and Dimorphos as point mass bodies. To have a more realistic model representing the dynamics in the Didymos system, orbital perturbations are added. Three orbital perturbations are of interest in this model: the gravitational perturbations of Didymos and Dimorphos and the Solar radiation pressure (SRP).

Due to the nature of the shapes of Didymos and Dimorphos, the gravitational potentials have to be adapted. The gravitational perturbation of Didymos will be derived using a spherical harmonic approach. The gravitational perturbation of Dimorphos will be considered by a closed-form gravitational potential of a constant density ellipsoid. An alternative orbital perturbation for Dimorphos will be implemented in section 5.2.

Finally, the Solar radiation pressure comes from the transfer of momentum from photos when they impact the spacecraft. This effect is important and has to be taken into consideration in the model.

2.2.1 Gravitational perturbation of Didymos

The gravitational potential U must respect Laplace's equation $\nabla^2 U = 0$. The spherical harmonics representation comes from solving Laplace's equation and are defined in spherical coordinates (ξ_i, ϕ, λ). The change of coordinates between Cartesian and spherical coordinates is done by :

$$\begin{cases} \xi_i = \sqrt{(r_x - r_i)^2 + r_y^2 + r_z^2} \\ \phi = arcsin\left(\frac{r_z}{\xi_i}\right) \\ \lambda = arctan\left(\frac{r_y}{r_x}\right) \end{cases} \tag{2.7}$$

Currently, zonal harmonics are considered for Didymos. Zonal harmonics are function of ξ_i and ϕ.

In spherical coordinates, the gravitational potential up to degree N of body i is given by

$$U(\xi_i, \phi) = \frac{Gm_i}{\xi_i} \sum_{n=0}^{N} J_n \left(\frac{R_i}{\xi_i}\right)^n P_n(\sin(\phi)) \tag{2.8}$$

Where P_n are the Legendre polynomial of degree n, R_i is the radius of the sphere around body i and J_n are the harmonic coefficients of degree n.

The harmonic coefficients are provided by GMV and summarized in table 2.1

J_2	-0.011432722
J_4	0.004583058

Table 2.1: Didymos spherical harmonic coefficients

Equation (2.8) can be written for Didymos using the harmonics coefficients in Table 2.1 as

$$U_1(\xi_1, \phi) = \frac{Gm_1}{\xi_1} \left(1 + J_2 \left(\frac{R_1}{\xi_1}\right)^2 P_2(\sin(\phi)) + J_4 \left(\frac{R_1}{\xi_1}\right)^4 P_4(\sin(\phi))\right) \tag{2.9}$$

where $R_1 = 399$ m (from Table 1.1), $\xi_1 = \sqrt{(r_x - r_1)^2 + r_y^2 + r_z^2}$ and the Legendre polynomials [32] are given for $x = \sin(\phi) = \frac{r_z}{\xi_1}$ by

$$\begin{cases} P_2 = \frac{1}{2}(3x^2 - 1) \\ P_4 = \frac{1}{8}(35x^4 - 30x^2 + 3) \end{cases} \tag{2.10}$$

The acceleration in synodic frame is given by taking the partial derivative of the gravitational potential (2.9):

$$\begin{cases} U_{1,x} = \frac{\partial}{\partial r_x} U_1(\xi_1, \phi) \\ U_{1,y} = \frac{\partial}{\partial r_y} U_1(\xi_1, \phi) \\ U_{1,z} = \frac{\partial}{\partial r_z} U_1(\xi_1, \phi) \end{cases} \tag{2.11}$$

2.2.2 Gravitational perturbation of Dimorphos

The gravitational perturbation considered for Dimorphos is a closed-form gravitational potential of a constant density ellipsoid and is derived in [26]. A constant density ellipsoid with semi-major axis $\gamma \leq \beta \leq \alpha$ and defined by the equation $(\frac{x}{\alpha})^2 + (\frac{y}{\beta})^2 + (\frac{z}{\gamma})^2 \leq 1$, see Figure 2.2

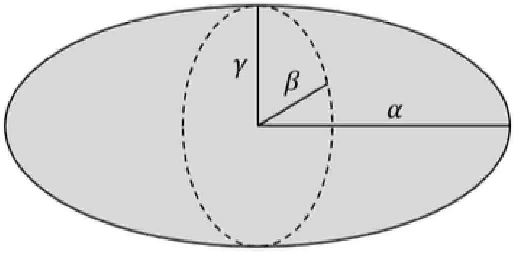

Figure 2.2: Tri-axial ellipsoid [26].

The position of the spacecraft relative to the center of mass of Dimorphos is defined by

$$\boldsymbol{r}_{moon} = (r_x - r_2)\hat{\boldsymbol{e}}_r + r_y\hat{\boldsymbol{e}}_\theta + r_z\hat{\boldsymbol{e}}_3 \tag{2.12}$$

The gravitational potential of the ellipsoid is then defined as

$$U_2(\boldsymbol{r}_{moon}) = -\frac{3\mu}{4}\int_{\lambda(\boldsymbol{r}_{moon})}^{\infty}\phi(\boldsymbol{r}_{moon}, u)\frac{du}{\Delta(u)} \tag{2.13}$$

$$\phi(\boldsymbol{r}_{moon}, u) = \frac{(r_x - r_2)}{\alpha^2 + u} + \frac{y^2}{\beta^2 + u} + \frac{z^2}{\gamma + u} - 1 \tag{2.14}$$

$$\Delta(u) = \sqrt{(\alpha^2 + u)(\beta^2 + u)(\gamma^2 + u)} \tag{2.15}$$

The acceleration in synodic frame is given by taking the partial derivative of the potential

$$\begin{cases} U_{2,x} = -\frac{3\mu(r_x - r_2)}{2}\int_{\lambda(\boldsymbol{r}_{moon})}^{\infty}\frac{du}{(\alpha^2+u)\Delta(u)} \\ U_{2,y} = -\frac{3\mu(r_y)}{2}\int_{\lambda(\boldsymbol{r}_{moon})}^{\infty}\frac{du}{(\beta^2+u)\Delta(u)} \\ U_{2,z} = -\frac{3\mu(r_y)}{2}\int_{\lambda(\boldsymbol{r}_{moon})}^{\infty}\frac{du}{(\gamma^2+u)\Delta(u)} \end{cases} \tag{2.16}$$

2.2.3 Solar radiation pressure

A simple SRP model is developed by adding the acceleration acting on the spacecraft by the solar radiations. The spacecraft is considered as having a surface perpendicular to the Sun. The acceleration exerted on Juventas by the Sun is expressed as, from [5] :

$$\boldsymbol{a}_{SRP} = -p_{SR@1AU}\frac{\boldsymbol{r}_{sc-sun}}{||\boldsymbol{r}_{rc-sun}||^3}(AU)^2C_r\frac{A}{m} \tag{2.17}$$

where $p_{SR@1AU} = 4.5e^{-6}$ N/m^2 is the pressure exerted by the Sun on the spacecraft at 1 AU. AU is the astronomical unit constant[1]. $\frac{A}{m} = 1/30$ m^2/kg is the area to mass ratio of the spacecraft. $C_r = 1.5$ is the reflectivity coefficient.

2.2.4 Perturbed Circular-Restricted Three Body Problem

The equations of motion (2.6) presented in section 2.1 can be adapted by adding orbital perturbations. The gravitational potential of the point mass Didymos and Dimorphos are replaced by the new gravitational perturbations U_1 and U_2. The perturbed equations of motion now become :

$$\begin{cases} \ddot{r}_x = 2\dot{r}_y\omega + r_x\omega^2 - U_{1,x} - U_{2,x} + a_{SRP_x} \\ \ddot{r}_y = -2\dot{r}_x\omega + r_y\omega^2 - U_{1,y} - U_{2,y} + a_{SRP_y} \\ \ddot{r}_z = -U_{1,z} - U_{2,z} + a_{SRP_z} \end{cases} \tag{2.18}$$

The validation of the PCR3BP was made by Vanhalst and Hanon (2020) and will not be shown here again. In this thesis, the PCR3BP is thus considered as validated and can be used to find landing trajectories.

2.3 Numerical integration

The perturbed equations of motion derived in section 2.2.4 can be solved numerically. A numerical tool is developed in Matlab to compute propagated trajectories and is called a Propagator.

The equations of motion are numerically integrated using the solver *ode113* in Matlab with a relative error tolerance of 10^{-16} and an absolute relative error tolerance of 10^{-17}. *ode113* is a multi step solver which means it needs solutions at preceding time steps to compute the current solution. It is based on a Adams-Bashforth-Moulton method. This solver is recommended for orbital mechanics problems as it can solve efficiently problems with high tolerance [8].

The positions of the Sun, Didymos and Dimorphos are accessed using SPICE kernels dataset. SPICE also provide a wide range of functions that can be used in Matlab to perform different computations and transformations of SPICE kernels.

Finally, the parameters considered in the model for the Didymos system are summarized on table 2.2. These parameters were used by Vanhalst and Hanon

[1] 1 AU is defined as exactly 149597870700 m

(2020) in their model and have since been updated. A new validation with the updated parameters will be performed in Chapter 5.

Parameters	**Designation**	**Value**
Total mass	m_{tot}	$5.278e^{11}$ kg
Mass parameter	μ	0.0093
Distance between Didymos and Dimorphos	r_{12}	1180 m
Dimorphos principal axes x;y;z	$x_r; y_r; z_r$	206, 158, 132 m

Table 2.2: Parameters of the Didymos system.

Chapter 3

Computing landing trajectories

In this chapter, a review of the method presented by Vanhalst and Hanon (2020) to compute landing trajectories is proposed. The direct landing strategy is presented through a backward propagation to generate a set of trajectories. After finding optimal trajectories, a Monte Carlo analysis is performed. This is a necessary introduction to Chapter 4 where a numerical optimization of the computation of landing trajectories in term of performance is proposed and studied.

3.1 Landing trajectories

The landing phase analysis is described in the Juventas Mission Analysis Report [15] and a similar landing strategy will be explained in this thesis.

The landing phase starts after the Proximity Observations Phase (POP) as described in Chapter 1. In this context, direct landing strategies are studied where one DeltaV maneuver is performed while leaving the 2 km SSTO [15].

Based on the Juventas Mission Analysis report [15], a set of parameters to take into account when selecting landing trajectories are discussed: the landing date, the landing velocity, the transfer duration, the phase angles of Juventas with respect to Didymos and Dimorphos and the deltaV maneuver when leaving the SSTO. The landing date is on the 09 August of 2027. These parameters are summarized in Table 3.1.

Parameters	Threshold
Landing velocity	≥ 8 cm/s
Duration of trajectory	< 6 hours
Phase Angle of Juventas w.r.t. Didymos	$< 90°$
Phase Angle of Juventas w.r.t. Dimorphos	$< 90°$
DeltaV	< 19.9 cm/s

Table 3.1: Selection criteria of landing trajectories, from [15].

The illumination condition is crucial in the mission's success as visual navigation is needed. The landing velocity is important as it increases the feasible area of landing. A maximum velocity of 10 cm/s is recommended. Velocity below 8 cm/s are discarded as the feasible area for landing on the surface is too small.

3.1.1 Backward propagation

A backward propagation is performed to generate landing trajectories starting from the surface of Dimorphos until reaching the 2 km SSTO. It means that trajectories are propagated backward in time with initial conditions on the surface of Dimorphos until one of the two following criteria is met : the distance between the trajectory and the SSTO is less than 4 meters or the propagation has reached 12 hours.

A grid of possible landing sites on the surface of Dimorphos is generated to study the landing phase. The landing sites are separated by a spread of 10° in longitude and latitude, see Figure 3.1. The 0° latitude is chosen to be relative to the equator of Dimorphos, i.e perpendicular to its rotation axis $\hat{\boldsymbol{e}}_3$. The positive longitudes are chosen through the direction of the velocity and the positive latitudes are chosen to be coincident with the direction of the pole of Dimorphos [15].

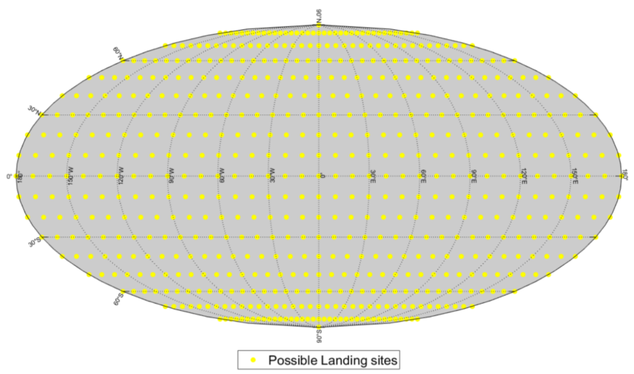

Figure 3.1: Landing sites generated on the surface of Dimorphos, from [14].

For the generated possible landing sites, the velocity and landing epoch are varied :

- Landing velocities of 8, 9 and 10 cm/s are considered.
- The landing dates between the 09-August-2027 at 14:15:00 and 10-August-2027 02:15:00 are studied. The dates are considered to fulfill a full orbit of Dimorphos which has a period of 11.92. Each landing epoch are separated by 15 min so a total of 49 epochs are considered during the chosen period.

However, landing epochs between 09-August-2027 18:15:00 and 09-August-2027 23:45:00 have to be discarded from the analysis as they do not respect the illumination conditions or are in the eclipse zone of Didymos. It means that 23 epochs are rejected and thus a total of 26 different landing epochs are considered for the backward propagation.

The latitude and longitude are separated by 10° so 703 different landing sites are considered on the surface of Dimorphos. Since there are 3 landing velocities, a total of 2109 different possibilities are considered at each time epoch. For 26 time epochs, the amount of possibilities tested is $54,834$.

It is also important to note that many landing sites will also be discarded from the analysis as they do not respect the illumination condition. In fact, the number of computed trajectories is almost half the $54,834$ considered. The true number of trajectories considered is $26,079$ when the illumination condition is respected.

From all the possibilities tested for the backward propagation, a total of 31 trajectories were found respecting the selection criteria from table 3.1. To assess the robustness of the found trajectories, a Monte Carlo analysis is needed.

3.1.2 Monte Carlo analysis

A Monte Carlo analysis on the 31 trajectories found by backward propagation is performed. The following uncertainties were studied :

- Uncertainties on the position and velocity on the SSTO (on-board estimation) that arise from the GNC (Guidance, Navigation, Control).
- Uncertainties on the one deltaV maneuver while leaving the SSTO that arise from the thrusters uncertainties.

These uncertainties are summarized in table 3.2.

Parameters	1σ uncertainty	Unit
SSTO uncertainties		
Position uncertainty	10	m
Velocity uncertainty	0.2	mm/s
Maneuver uncertainties		
Impulse magnitude	5	%
Impulse orientation	1.5	degree

Table 3.2: Uncertainties from GMV, [14]

For the Monte Carlo analysis, the initial conditions of the 31 trajectories on the SSTO are varied to respect the uncertainties from table 3.2 and propagated forward in time until landing on Dimorphos or being lost in space. Thus, many relevant information can be derived from the Monte Carlo Analysis such as:

- The success rate : percentage of trajectories impacting Dimorphos.
- Global success rate : percentage of trajectories that landed and rested on Dimorphos after bouncing.
- Impact velocity : velocity when impacting Dimorphos
- Transfer time : duration of the descent until landing on Dimorphos
- Impact angle : angle of impact on Dimorphos.
- ...

A convergence analysis on the design of these parameters has been made by Vanhalst and Hanon (2020). They showed that 2500 samples are sufficient to ensure the convergence of the results.

Many interesting discussions can be made on the design of the trajectory parameters. For instance, higher success rates were found when minimizing the transfer time and the landing velocity.

Thus, after the Monte Carlo analysis, Vanhalst and Hanon (2020) found found two trajectories considered as optimal with a selection criteria on a combination of high success rate and low settling time.

From the Monte Carlo, 2500 samples have to be computed for the 31 trajectories. So a total $77,500$ trajectories are propagated.

3.1.3 Conclusion

It can be seen that for the backward propagation and Monte Carlo analysis, a huge set of trajectories have to be computed. An investigation of an optimized integrator will be assessed in the next Chapter to compute these propagated trajectories efficiently and quickly.

Chapter 4

Optimization in Matlab and numerical integration methods

The landing strategies were presented in Chapter 3. In this Chapter, the current performance of the code of Vanhalst and Hanon (2020) to compute propagated trajectories is discussed as well as how improvements can be made.

Then, a numerical tool to compute propagated trajectories quickly and efficiently is investigated. First, a variable step Runge-Kutta Felhberg integrator is presented and validated using results from *ode113*. Then, a vectorized Runge-Kutta Felhberg integrator is designed and its performances are tested with *ode113*.

Finally, the vectorized integrator is implemented in the code made by Vanhalst and Hanon (2020) and the new performances are discussed.

4.1 Optimisation in Matlab

In Chapter 3, methods to compute landing trajectories were proposed and it resulted that many trajectories have to be propagated. Indeed, for the backward propagation and the Monte Carlo simulations a total of $26,079$ and $77,500$ trajectories have to be computed, respectively. Such computations can take a lot of time. The computational time of the two methods currently implemented by Vanhalst and Hanon (2020) are depicted below:

- Backward propagation : It takes on average 19.5 minutes to compute the trajectories at each 15 minutes epoch with a total of 8.46 hours for 26 epochs.
- Monte Carlo simulation : It takes on average 25 minutes to compute 2500 samples with a total of more than 12.5 hours for the 31 trajectories.

It is thus of great interest to have a numerical tool able to propagate many trajectories efficiently and quickly for further similar studies. In this context, an optimisation of the code developed by Vanhalst and Hanon (2020) as well as the investigation of an efficient integrator will be proposed in the next sections.

4.1.1 Vectorization

Matlab is designed and optimized to favor operations taking into account matrices and vectors. The concept of revising a code based on loops into a vector-oriented code in order to use Matlab matrix and vector operations is called vectorization. Vectorization is important because it improves code performance, that is, vectorizing code runs faster than code containing loops [20]. Vectorization is thus an extremely powerful tool and should be used when trying to achieve better performance.

The code developed by Vanhalst and Hanon (2020) to compute propagated trajectories (backward propagation and Monte Carlo simulations) is a loop-based code where, at each iteration, a new initial value problem (IVP) is solved using *ode113*. The expensive operation here is solving the IVP with *ode113* which takes approximately 99% of the computational time in Matlab. The idea is to vectorize the computation of the IVP. In this context, a numerical integrator will be presented in the next section as well as its vectorized implementation.

4.2 Numerical integration

The first approach considered was to build a simple Runge-Kutta 4 integrator and vectorize it. However, for some trajectories the time steps had to be extremely small which would increase considerably the computational time and thus make the integrator not sufficient enough. Indeed, when working with three body problems and more precisely in the restricted three body problem, the time steps have to be very small when the third body approaches a singularity [13] resulting in a high variation in velocity.

In this context, a variable step size integrator will be designed in this section based on a Runge-Kutta Fehlberg method. Then a vectorized version will be proposed.

4.2.1 Runge-Kutta Felhberg

Runge-Kutta Felhberg (RKF) method is an adaptive step size numerical integration method. In this thesis, the Runge-Kutta 45 (RKF45) method [9] will be developed where at each step, two different approximations of solutions are compared: a fourth order method with a fifth order method. The time step is reduced until the required approximation is achieved. The coefficients of the method also known as Butcher tableau are given in table 4.1

0						
1/4	1/4					
3/8	3/32	9/32				
12/13	1932/2197	−7200/2197	7296/2197			
1	439/216	−8	3680/513	−845/4104		
1/2	−8/27	2	−3544/2565	1859/4104	−11/40	
	16/135	0	6656/12825	28561/56430	−9/50	2/55
	25/216	0	1408/2565	2197/4104	−1/5	0

Table 4.1: Butcher tableau.

From the Boutcher tableau, at iteration n the RKF45 method is given by

$$k_1 = f(t_n, y_n) \tag{4.1}$$
$$k_2 = f(t_n + \frac{1}{4}h, y_n + \frac{1}{4}k_1) \tag{4.2}$$
$$k_3 = f(t_n + \frac{3}{8}h, y_n + \frac{3}{32}k_1 + \frac{9}{32}k_2) \tag{4.3}$$
$$k_4 = f(t_n + \frac{12}{13}h, y_n + \frac{1932}{2197}k_1 - \frac{7200}{2197}k_2 + \frac{7296}{2197}k_3) \tag{4.4}$$
$$k_5 = f(t_n + h, y_n + \frac{439}{216}k_1 - 8k_2 + \frac{3680}{513}k_3 - \frac{845}{4104}k_4) \tag{4.5}$$
$$k_6 = f(t_n + \frac{1}{2}h, y_n - \frac{8}{27}k_1 + 2k_2 - \frac{3544}{2565}k_3 + \frac{1859}{4104}k_4 - \frac{11}{40}k_5) \tag{4.6}$$

Here $f(t, y)$ is the equations of motion found in section 2.1 such that $dy/dt = f(t, y)$.

Then the approximation of the solution is made by a method of order 5 and 4

$$y_{n+1} = y_n + h(\frac{16}{135}k_1 + \frac{6656}{12825}k_3 + \frac{28561}{56430}k_4 - \frac{9}{50}k_5 + \frac{2}{55}k_6) \tag{4.7}$$
$$y^*_{n+1} = y_n + h(\frac{25}{216}k_1 + \frac{1408}{2565}k_3 + \frac{2197}{4104}k_4 - \frac{1}{5}k_5) \tag{4.8}$$

The error estimate is

$$\epsilon = |y_{n+1} - y^*_{n+1}| \tag{4.9}$$

The optimal step size h_{opt} is determined by the current step h by

$$h_{opt} = \begin{cases} 0.9h\left(\frac{\epsilon_0}{\epsilon}\right)^{1/5} & \text{if } \epsilon \geq \epsilon_0 \\ 0.84h\left(\frac{\epsilon_0}{\epsilon}\right)^{1/4} & \text{if } \epsilon < \epsilon_0 \end{cases} \tag{4.10}$$

where ϵ_0 is the desired accuracy. If $\epsilon \geq \epsilon_0$, the step size is reduced at the current step, and if $\epsilon < \epsilon_0$ the step size has to be increased in the next step.

Validation

The RKF45 method developed previously has been implemented in Matlab and can be validated using the results of *ode113*. For the validation, the initial conditions on the trajectory in synodic frame are the following

x [m]	y [m]	z [m]	v_x [m/s]	v_y [m/s]	v_z [m/s]
1369.810	1336.772	-18.969	0.098	-0.126	-0.07

and an initial date on the 2027 AUG 09 08:00:00 is considered. The trajectory will be propagated during 12 hours in the Didymos system with an initial time step of 20 s and a relative tolerance of $1e^{-8}$.

The relative errors (%) through time in position and velocity with *ode113* are shown in Figure 4.1. It can be seen that, in both cases, the errors are extremely small, of order less than $1e^{-7}$%. The maximum and minimum errors as well as the error at the last step of the trajectories for the position and velocity are summarized in Table 4.2.

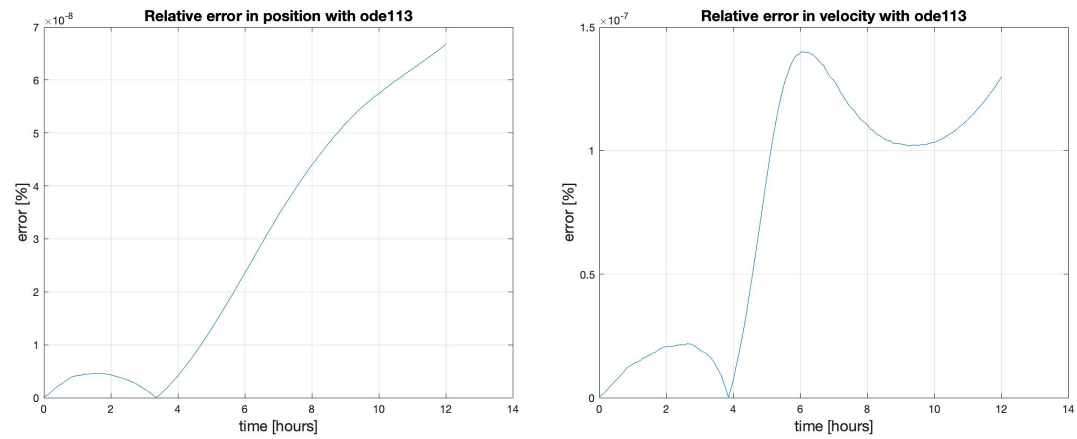

(a) Relative error in position. (b) Relative error in velocity.

Figure 4.1: Relative errors between RKF45 and *ode113*.

	Position	**Velocity**
maximum relative error (%)	$6.6861e^{-8}$	$1.4002e^{-7}$
minimum relative error (%)	$8.8265e^{-11}$	$1.4299e^{-10}$
relative error at the last step of the trajectory (%)	$6.6861e^{-8}$	$1.3000e^{-7}$

Table 4.2: Relative errors comparison with *ode113*.

The velocity and time steps are shown in Figure 4.2 to highlight the importance of the adaptive time step method. Indeed, as explained previously, the time steps and the velocity are related. The RKF45 method adapts the time step when the change of velocity is high. For instance, here the time step was reduced up to 2.8582 s.

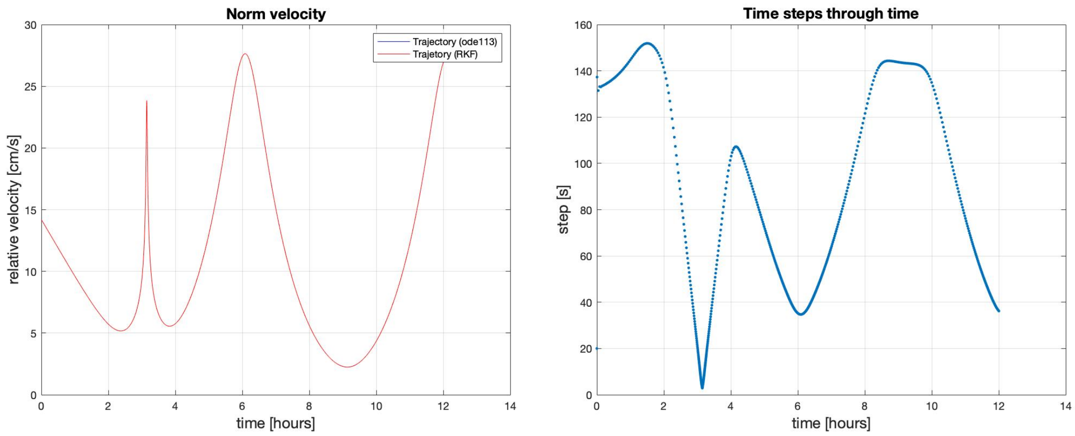

(a) Velocity in synodic frame.

(b) Time steps RKF45.

Figure 4.2: Evolution of the velocity and time steps.

As a conclusion, with such low errors the RKF45 method is considered validated and in agreement with the expected results of *ode113*. Next, a vectorized version of the RKF45 will be introduced.

4.2.2 Vectorized Runge-Kutta Fehlberg

The goal of this chapter is to present an optimised numerical integrator able to compute many trajectories efficiently. The numerical method that has been designed previously is a RKF45 method that is currently validated to compute one

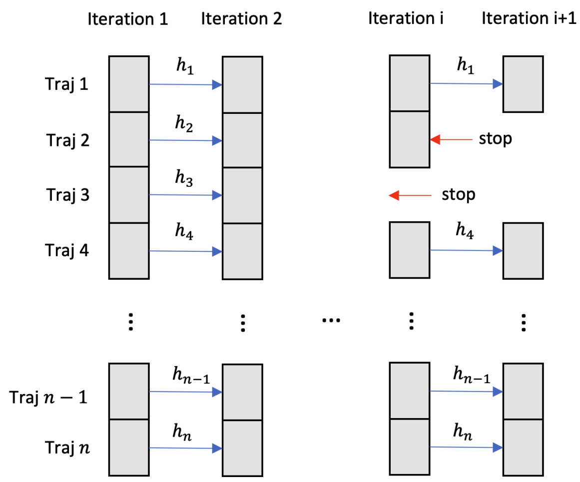

Figure 4.3: Representation of vectorized RKF45.

trajectory. Now the analysis is extended to build vectorized version of RKF45 to reach better performances.

The main idea behind the vectorized RKF45 is to compute each trajectory in parallel in huge matrices. At each iteration, every trajectory is computed at the same time for a time step that is specific to each trajectory, as seen in Figure 4.3. This can be done using logical array indexing in Matlab.

At each iteration i, the $k_1, ...k_6, y^*_{i+1}, y_{i+1}$ and the error ϵ is computed. Using logical array indexing, the conditions $\epsilon \geq \epsilon_0$ and $\epsilon < \epsilon_0$ can represent at which index the array satisfies these conditions. The $h_1, h_2, ..., h_n$ from Figure 4.3 are computed simultaneously but with different step sizes for n trajectories. The same method is used to stop the integration of a specific trajectory when it reached 12 hours (or any other stop conditions such as landing on Dimorphos). When reaching a stopping condition, the logical index of the trajectory will simply be considered as a 0 (false) and will not be used anymore. Only the trajectories with logical indices 1 (true) will be taken into consideration.

The process is vectorized at every step which makes it very fast and is scalable to any number of trajectories until reaching the 64-bit limit of Matlab.

Validation

The vectorized RKF45 method developed in this section will now be validated and compared to *ode113* in Matlab. A set of 1000 randomized initial conditions will be propagated during 12 hours for an initial date on the 2027 AUG 09 08:00:00. The tolerance is set to $1e^{-8}$ and an initial time step of 20 s is taken.

The validation will be made by comparing the maximum relative error in position and velocity along each trajectory computed by the vectorized RKF45 method and *ode113* as shown in Figure 4.4. The maximum and mean of the relative errors are summarized in Table 4.3.

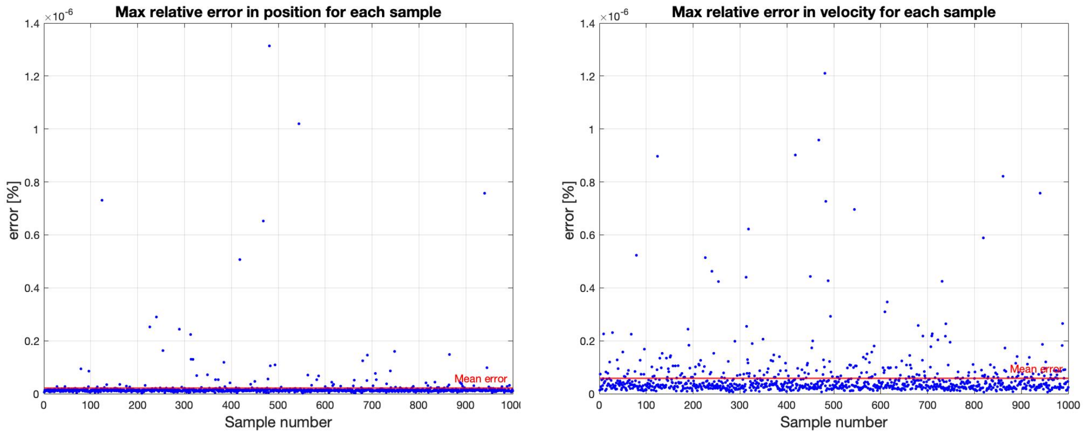

(a) Maximum relative error in position. (b) Maximum relative error in velocity.

Figure 4.4: Maximum relative error of each sample.

	Position	**Velocity**
maximum of maximum relative errors (%)	$1.3139e^{-6}$	$1.2103e^{-6}$
mean of maximum relative errors (%)	$1.4757e^{-}7$	$3.5609e^{-7}$

Table 4.3: Maximum relative errors comparison with *ode113*.

As it can be seen from Figure 4.4 and Table 4.3, the errors are relatively low with a maximum error of order $1e^{-6}$ in position and velocity. The mean relative error of all the trajectory is of order $1e^{-7}$ in both position and velocity. With such low errors for the chosen tolerance, the vectorized RKF45 method can be considered as validated and its performance will be assessed.

Performance

The vectorized RKF45 method has been validated and thus it is of great interest to finally test to computational time of the developed vectorized integrator against loop-based *ode113* code.

Similarly as the validation, a set of random initial conditions are generated on the 2027 AUG 09 08:00:00 and the number of samples is varied. In Figure 4.5a the computational time of the two methods is shown and in Figure 4.5b only the vectorized RKF45 performance is shown.

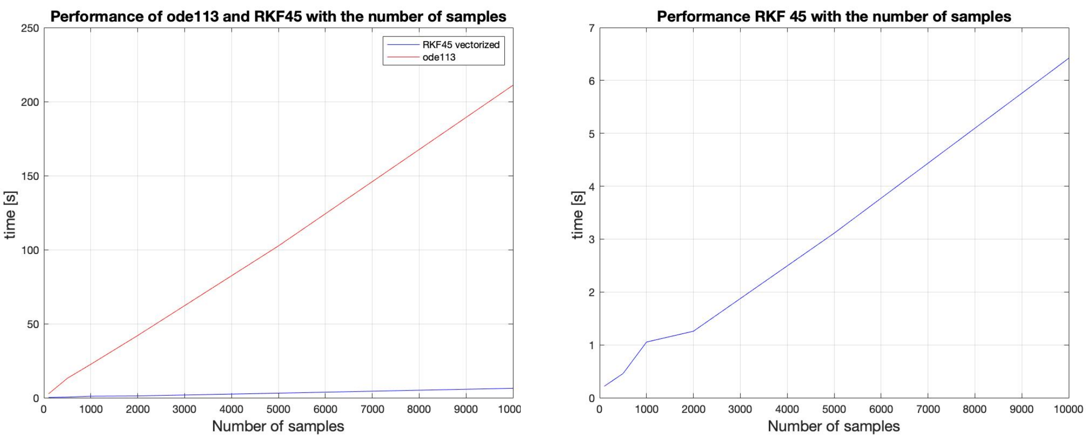

(a) ode113. (b) Vectorized RKF45.

Figure 4.5: Computational time with the number of samples.

From Figure 4.5 it can be seen that vectorized RKF45 performs much better than loop-based *ode113*. In both cases, the computational time is linear with the number of samples. The vectorized RKF45 code is on average between 20 to 30 faster than loop-based *ode113* which is a significant improvement. Some reference values are summarized in Table 4.4.

Number of samples	**Vectorized RKF45**	**ode113**
100	0.2372 s	2.6262 s
500	0.4434 s	13.3931 s
1000	1.0554 s	23.3702 s
2000	1.2740 s	44.0963 s
5000	3.7736 s	109.9655 s
10 000	8.0959 s	211.0196 s
50 000	55.1581 s	17.4521 min
100 000	114.4928 s	32.7891 min

Table 4.4: Computational time comparison with *ode113*.

4.3 Conclusion

The vectorized RKF45 method performs on average between 20 to 30 times better than simple loop-based ode113 code. Its performance is now discussed when compared with the loop-based code developed by Vanhalst and Hanon (2020) for the backward propagation and the Monte Carlo simulations.

In the loop-based code, the backward propagation took on average 19.5 min for one time epoch to a total of more than 8 hours for the 26 epochs. Thanks to the vectorized RKF45 method, the complete backward propagation takes 4.32 minutes which is 111 faster.

For the Monte Carlo simulations, it took on average 25 minutes to compute 2500 samples to a total of more than 12.5 hours for the 31 trajectories considered. With the vectorized RKF45 method, it takes on average 8.9987 s to compute 2500 samples per simulation. The 31 trajectories are computed in 4.65 minutes which is more than 161 times faster.

A significant improvement is observed. More advanced studies can be performed to find new optimal trajectories using the backward propagation and the Monte Carlo analysis. More trajectories could be computed to achieve more precise results without time constraints.

Chapter 5

Landing trajectory analysis

In the last few sections, numerical tools to find propagated trajectories were studied. From these propagated trajectories, optimal trajectories were found based on strict selection criteria. In this chapter, a nominal trajectory is provided by GMV. As some parameters have been updated, the Matlab Propagator is again validated with this trajectory and a new orbital perturbation is added.

After that, a braking maneuver is added during the descent to reduce the landing velocity. The braking maneuver will be implemented on the nominal trajectory.

Until now, Dimorphos has been considered as a triaxial ellipsoid. In this chapter, shape models are introduced to model Dimorphos. A new landing strategy is developed to land on arbitrary shape models.

Finally a simple bouncing model is presented. The bouncing model will also be developed to be performed on shape models.

5.1 Nominal trajectory

The nominal trajectory is provided by GMV. In their approach two landing strategies were discussed : direct landing and indirect landing through L2. In this thesis, only the direct landing strategy is considered. To generate the nominal trajectory, GMV used a similar approach as the one presented in Chapter 4. They performed a backward propagation from Dimorphos until the SSTO distance is reached. In this case, the chosen SSTO distance is 2km.[11]

For the backward propagation, the initial conditions (at landing point) on the surface of Dimorphos shall meet the following requirements [11] :

- Location on surface : Longitude $\in [-180, 180]^\circ$ and Latitude $\in [-90, 90]^\circ$
- Landing velocity (in synodic reference frame) : $|v_{land}| \in [5, 10]$ cm/s and $\frac{\vec{v}_{land}}{|v_{land}|}$ normal to surface
- Maximum propagation of 12 hours.

Using these conditions, a set of trajectories are propagated backward in time from the surface of Dimorphos until the SSTO is reached. GMV selected the nominal trajectory based on a combination of shortest duration, minimum deltaV and minimum landing velocity [29].

This trajectory will be the building block of the next few sections. From now on, this thesis will use this trajectory.

The nominal trajectory has been given in J2000Ecliptic frame (inertial frame). Using a frame transformation between this inertial and synodic reference frame (see Appendix A for more information about this transformation), the nominal trajectory is shown in Figure 5.1 in the synodic reference frame.

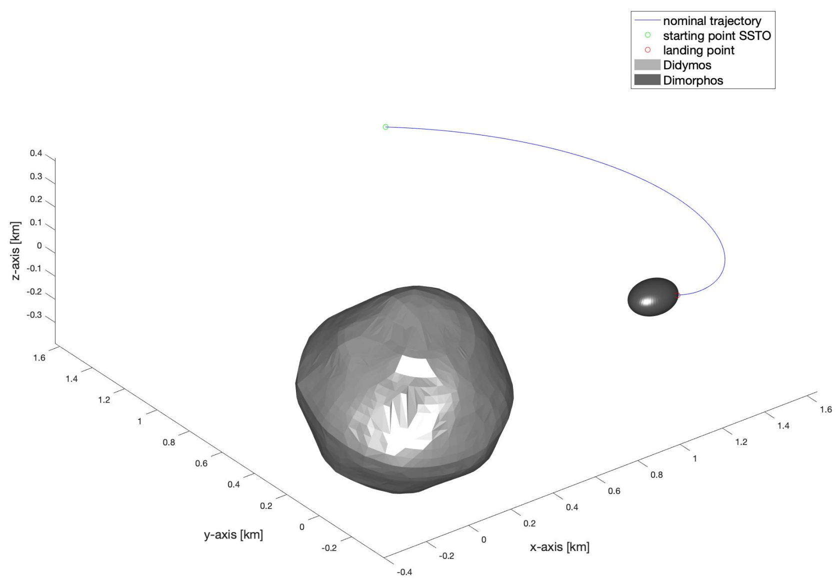

Figure 5.1: Nominal trajectory in synodic reference frame.

The nominal trajectory has the following characteristics :

- Departure time (leaving SSTO): 04-Jun-2027 19:49:25
- Final time (landing on Dimorphos) : 05-Jun-2027 01:56:05
- Duration of the trajectory : 6.11 [hours]
- Velocity at impact : 7 [cm/s]
- Latitude at impact : 9.2333 [°]
- Longitude at impact : -44.5937 [°]

This trajectory has been computed by GMV using updated parameters on the mass and the distance between the centers of mass (CoM) of Didymos and Dimorphos. In the next section, an update on the mass and the distance between the two bodies is discussed. The Perturbed circular restricted three body problem (PCR3BP) model will then be validated again with the new parameters using this nominal trajectory.

5.1.1 Update on the parameters

Since the work of Vanhalst and Hanon (2020), some important parameters have been updated which completely changes the dynamics of the system. The latest parameters were presented in section 1.2 and are available in the Didymos reference model V5.5 [1]. Table 5.1 summarizes the updated parameters considered for the Didymos system.

Parameters	**Designation**	**Old value**	**Updated value**
Dimorphos principal axes x;y;z	$x_r; y_r; z_r$	206 m; 158 m; 132 m	208 m; 160 m; 133 m
Semi-major axis	r_{12}	1180 m	1190 m

Table 5.1: Updated parameters of the system.

The update in the semi-major axis results in a change in the total mass of the system. Indeed, at the moment, there are two well-known quantities in the system : the orbital period of Dimorphos T and the semi-major axis of the orbit r_{12}.

Under the assumption of Kepler's third law for point mass bodies:

$$T = 2\pi\sqrt{\frac{r_{12}^3}{G(m_1 + m_2)}} \tag{5.1}$$

Thus a change in r_{12} leads to a change in the masses of the system keeping the orbital period constant.

Solving equation (5.1) for $T = 11.921626$ h[1], $G = 6.6743 \times 10^{-11}$ m^{3}kg^{-1}s^{-2} gives a total mass of 5.4114×10^{11} kg.

5.2 New orbital perturbation

In Chapter 2, 3 orbital perturbations were considered : Solar radiation pressure, gravitational perturbations from Didymos and Dimorphos.

As shown in Chapter 2, the gravitational perturbation for Didymos is derived using a spherical harmonic approach while the gravitational perturbation for Dimorphos is derived using a closed-from gravitational potential of a constant density ellipsoid.

In the context of this thesis, an alternative gravitational perturbation for Dimorphos is presented. The new gravitational perturbation uses a spherical harmonic representation of the gravitational potential similar to the perturbation used for Didymos.

The gravitational potential is expressed in spherical coordinates (ξ_i, ϕ, λ). Recall that the change of coordinates between Cartesian and spherical coordinates in the synodic frame is the following :

$$\begin{cases} \xi_i = \sqrt{(r_x - r_i)^2 + r_y^2 + r_z^2} \\ \phi = arcsin\left(\frac{r_z}{\xi_i}\right) \\ \lambda = arctan\left(\frac{r_y}{r_x}\right) \end{cases} \tag{5.2}$$

In spherical coordinates, the gravitational potential up to degree N of body i is given by [18] :

$$U(\xi_i, \phi, \lambda) = \frac{Gm_i}{\xi_i} \sum_{l=0}^{N} \sum_{m=0}^{l} \left(\frac{R_i}{\xi_i}\right)^l P_{l,m}(\sin(\phi)) \Big(C_{l,m}\cos(m\lambda) + S_{l,m}\sin(m\lambda)\Big) \tag{5.3}$$

where $P_{l,m}$ are the associated Legendre polynomials and R_i the radius of the sphere around body i.

[1]From Didymos reference model V5.5 [1]

The matrices $\boldsymbol{C}$ and $\boldsymbol{S}$ provided by GMV are :

$$\boldsymbol{C} = \begin{bmatrix} 0 & 0 & 0 & 0 & 0 \\ 0 & 0 & 0 & 0 & 0 \\ -0.1325 & 0 & 0.0349 & 0 & 0 \\ 0 & 0 & 0 & 0 & 0 \\ 0.0429 & 0 & -0.0033 & 0 & 2.1810 \times 10^{-4} \end{bmatrix}, \quad \boldsymbol{S} = [0]_{5,5}$$

Considering matrices $\boldsymbol{C}$ and $\boldsymbol{S}$ in (5.3) as well as going up to order 4 for Dimorphos gives the following expression :

$$U(\xi_2, \phi, \lambda) = \frac{Gm_2}{\xi_2}\left(1 + \sum_{l=1}^{4}\sum_{m=0}^{l+1}\left(\frac{R_2}{\xi_2}\right)^l P_{l,m}(\sin(\phi))C_{l+1,m+1}\cos(m\lambda)\right) \tag{5.4}$$

where the only non zero elements are $(l = 2, m = \{0, 2\}), (l = 4, m = \{0, 2, 4\})$. The associated Legendre polynomials are given in table 5.2 for $x = \sin(\phi) = \frac{r_z}{\xi_2}$

$P_{2,0}(x) = \frac{1}{2}(3x^2 - 1)$	$P_{4,0}(x) = \frac{1}{8}(35x^4 - 30x^2 + 3)$
$P_{2,2}(x) = 3(1 - x^2)$	$P_{4,2}(x) = \frac{15}{2}(7x^2 - 1)(1 - x^2)$
	$P_{4,4}(x) = 105(1 - x^2)^2$

Table 5.2: associated Legendre polynomials [4].

The relative acceleration in synodic frame is given by taking the partial derivative of the gravitational potential.

$$\begin{cases} U_{2,x} = \frac{\partial}{\partial r_x}U(\xi_2, \phi, \lambda) \\ U_{2,y} = \frac{\partial}{\partial r_y}U(\xi_2, \phi, \lambda) \\ U_{2,z} = \frac{\partial}{\partial r_z}U(\xi_2, \phi, \lambda) \end{cases} \tag{5.5}$$

The partial derivatives are computed using symbolic computations in Matlab.

Next, the new perturbation will be validated using the new parameters. The comparison will be made between the nominal trajectory and the PCR3BP model presented in Chapter 2.

5.2.1 Validation

Two PCR3BP models are considered with two different orbital perturbations for Dimorphos: a closed form gravitational potential of a constant density ellipsoid (called gravity ellipsoid) and a spherical harmonic representation of the gravitational potential up to order 4 (called gravity order 4). These two gravity models can be validated using the nominal trajectory provided by GMV.

In their model, GMV used the gravitational pull of both bodies, a 3rd body influence of the sun, a 20th order gravity model for Didymos, a 4th order gravity model for Dimorphos and a solar radiation pressure model.

The nominal trajectory given by GMV contains 221 epochs where the time step is exactly 100 seconds. When leaving the 2 km SSTO, the initial date is on the 04-Jun-2027 19:49:25 and the initial conditions of the nominal trajectory in synodic reference frame are the following:

x [m]	y [m]	z [m]	v_x [m/s]	v_y [m/s]	v_z [m/s]
1162.2061	1628.0010	-3.1229	0.1189	-0.1181	0.0065

Both models are propagated on the 221 epochs using the initial conditions from the nominal trajectory. Figure 5.2 shows the propagated and nominal trajectories for these epochs. A more precise look is given in Figure 5.3 where the last 50 epochs are shown.

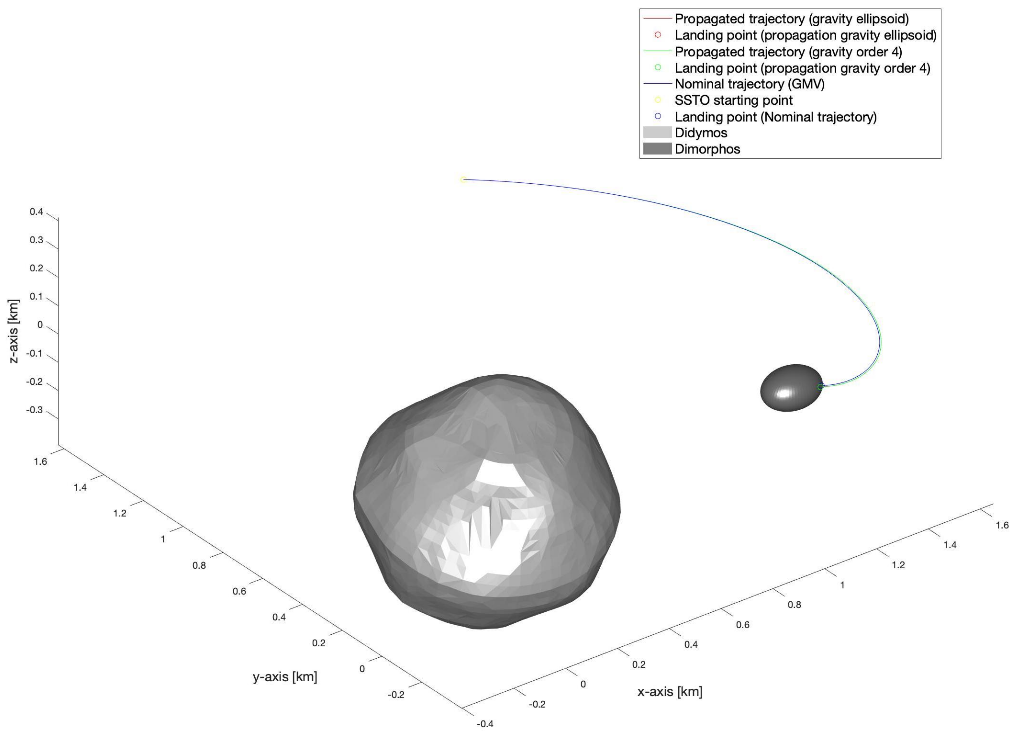

Figure 5.2: Comparison trajectories in synodic frame.

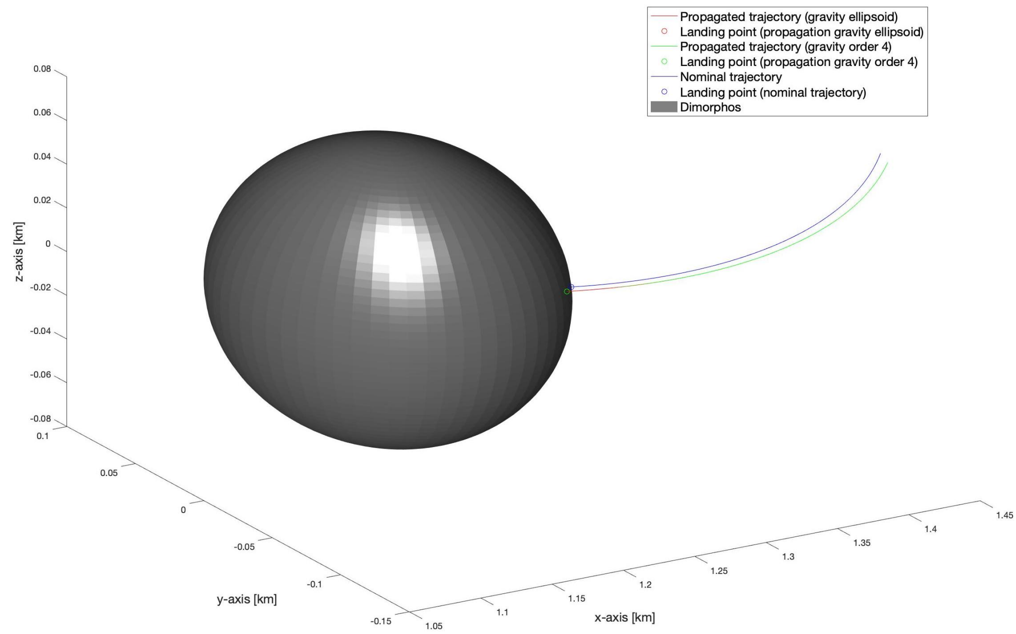

Figure 5.3: Zoom on the last 50 epochs.

In figure 5.3, a slight offset in position is apparent between the nominal and the propagated trajectories. The two propagated trajectories are looking very similar. The relative error in position between the nominal trajectory and both perturbed trajectories is shown in Figure 5.4a where the relative error is computed at each epoch. Throughout the trajectory the errors are quite small, less than one percent with a peak at 0.6521% for both models. The relative errors in velocity is shown in Figure 5.4b where it can be seen that it is less than two percent during the descent with a peak at 2.0173% for the gravity ellipsoid model and 2.0173% for the 4th order gravity model.

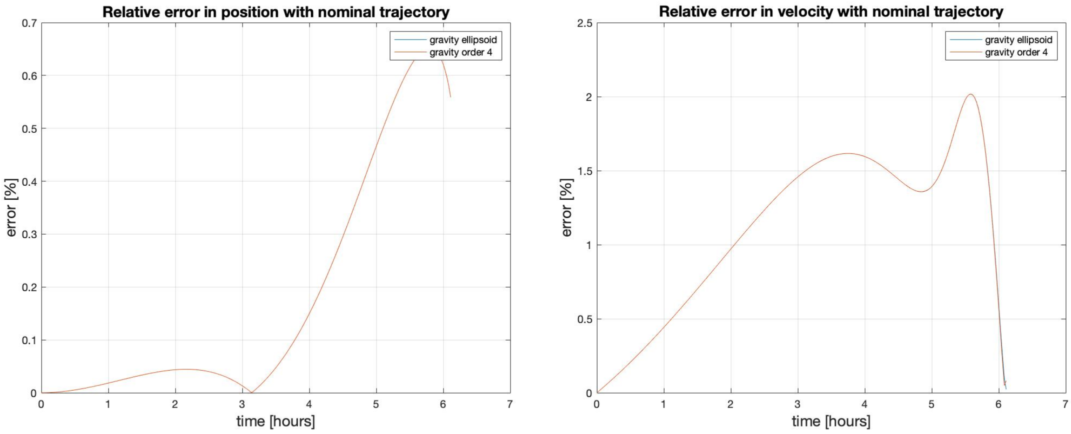

(a) Relative error in position.

(b) Relative error in velocity.

Figure 5.4: Comparison of the propagated trajectory and the nominal trajectory.

The landing velocities are summarized in table 5.3.

	Landing velocity	**Relative error**
Gravity ellipsoid model	6.9958 [cm/s]	0.0234%
Gravity order 4 model	6.9917 [cm/s]	0.0819%

Table 5.3: Landing velocity and relative error of both perturbed models.

Even though the errors are very small, the differences can come from the model itself. Indeed the implementation of the model by GMV is different than the one developed in this thesis. More precisely, in their model, GMV used the gravitational pull of both bodies, a 3rd body influence of the sun, a 20th order gravity model for Didymos, a 4th order gravity model for Dimorphos and a solar radiation pressure model whereas in the PCR3BP model, the solar pressure model and the gravitational perturbations of Didymos and Dimorphos are considered.

Looking at these results, the two gravity models developed in this thesis for Dimorphos seem very similar. A deeper comparison of the two orbital perturbations is made. Figure 5.5 compares the acceleration due to both perturbations on the trajectory as well as the relative errors between them.

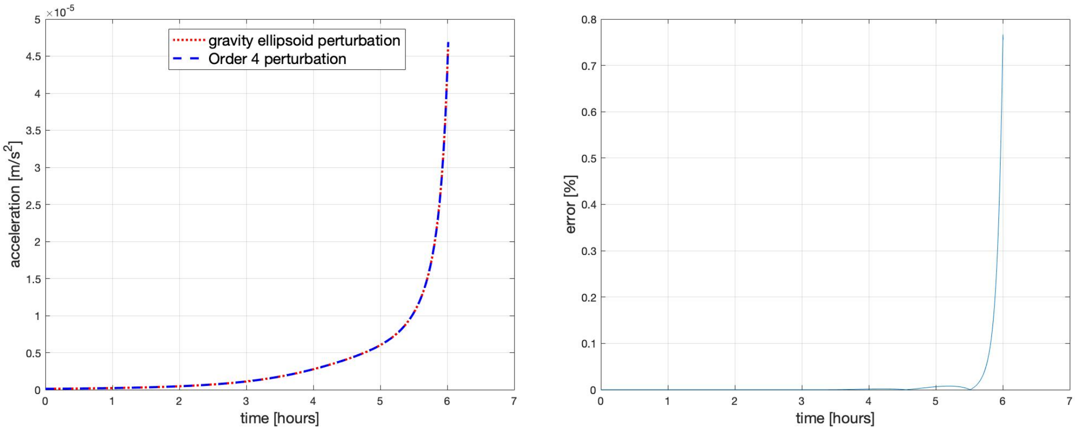

(a) Relative acceleration.

(b) Relative error in acceleration.

Figure 5.5: Comparison of the relative acceleration of both perturbations.

From Figure 5.5a, it can be seen that the acceleration grows over time as the spacecraft gets closer to Dimorphos. Looking at Figure 5.5b where the relative error between them is shown, it is exactly zero during the beginning of the propagation and reaches a maximum error of 0.7667% at the end of the trajectory when the spacecraft gets closer to Dimorphos. The results are consistent and the two gravity model are considered validated.

To conclude this section, the Matlab propagator developed with the new parameters and the two different perturbations is considered as validated.

5.3 Braking maneuver

As seen in the work of Vanhalst and Hanon (2020), high landing velocities can lead to lower landing success rate as the spacecraft could simply bounce off Dimorphos. Until now, one DeltaV maneuver was performed while leaving the SSTO. In this thesis, a second DeltaV maneuver is considered close to Dimorphos to reduced the impact velocity.

The braking maneuver is performed at GNC (Guidance, Navigation and control) level and is developed by GMV. When leaving the SSTO (at the beginning of the trajectory) the uncertainties on the position and velocity are huge. To reduce the uncertainties, GMV completed two correction maneuvers during the descent, before the final braking maneuver. After the two correction maneuvers, GMV provided the new dispersion.

In this thesis, a simpler implementation of the reaction control system (RCS) system of Juventas is implemented. In reality, this process is complex as the thrusters are pointing in multiple directions. Here, only one thruster in the direction of the maneuver is considered. A simple braking maneuver will be performed. The operation is reduced to a single force applied on the spacecraft in the opposite direction of the descent. The thrust is assumed constant at maximum capacity of the idealised unidirectional thruster.

5.3.1 Implementation

GMV proposed to perform the braking maneuver at a 50m distance from Dimorphos [10], after the dispersion in position and velocity.

The 1-σ knowledge in position and velocity in inertial frame at 50m (before braking maneuver) is provided by GMV and is available in table 5.4

Phase	**Position [m]**	**Velocity [mm/s]**
X	11.54	2.46
Y	9.04	1.22
Z	9.25	1.14

Table 5.4: 1-σ knowledge at 50m in the inertial frame

At the altitude of 50m, before the braking maneuver, a change of variable between the synodic frame and inertial frame is performed. Then the dispersion is done in inertial frame and another change of variable between the inertial and synodic frame is performed again.

At that altitude after dispersion, the total deltaV of the braking maneuver is computed for a target velocity of 2 cm/s in the opposite direction of the spacecraft pointing towards Dimorphos.

The deltaV can not be applied immediately due to the thruster's limitation. The maximum thrust of the thruster is 1mN. Knowing that the mass of Juventas is 12kg, the maximum acceleration available is known. Thus, at one time step, the maximum deltaV can be computed by

$$\max \Delta V = \frac{10^{-3}}{12} * dt$$

where dt is the time step at time t.

During the braking maneuver, at each time step, the maximum instantaneous deltaV is applied until the necessary deltaV of the maneuver has been applied.

The implementation of the braking maneuver can be summarized with the following algorithm:

1. The model is propagated until reaching 50m of altitude to Dimorphos.
2. The position and velocity are transformed in the inertial frame.
3. The position and velocity are dispersed with the 1-σ knowledge provided by GMV.
4. The position and velocity are transformed back in the synodic frame.
5. The deltaV of the braking maneuver is computed to have a target velocity of 2 cm/s toward Dimorphos.
6. At each time step, the maximum deltaV that can be applied respecting the thruster and mass limitations is computed.
7. The braking maneuver is completed when the whole deltaV has been applied.
8. The model is then propagated again until landing on Dimorphos.

5.3.2 Results

Two scenarios are considered where the dispersion is performed or not performed at 50m. When the dispersion is not performed, the nominal trajectory will be used for comparison. In the case of the dispersion on the position and velocity, 100 samples are generated and analyzed.

As an example, the last 50m of the nominal trajectory (without any maneuvers) and the trajectory resulting from the braking maneuver without dispersion is shown in Figure 5.6.

The objective of the braking maneuver is to reduce the landing velocity. On this example, the norm of the velocity in synodic frame is shown in Figure 5.7. It can be seen that during the braking maneuver, the minimum velocity reached is 2.6783 cm/s. After that, the propagation continues and the spacecraft simply falls on Dimorphos without additional correction maneuvers.

At the altitude of 50m, the velocity of Juventas is 5.0433 cm/s. Since the target

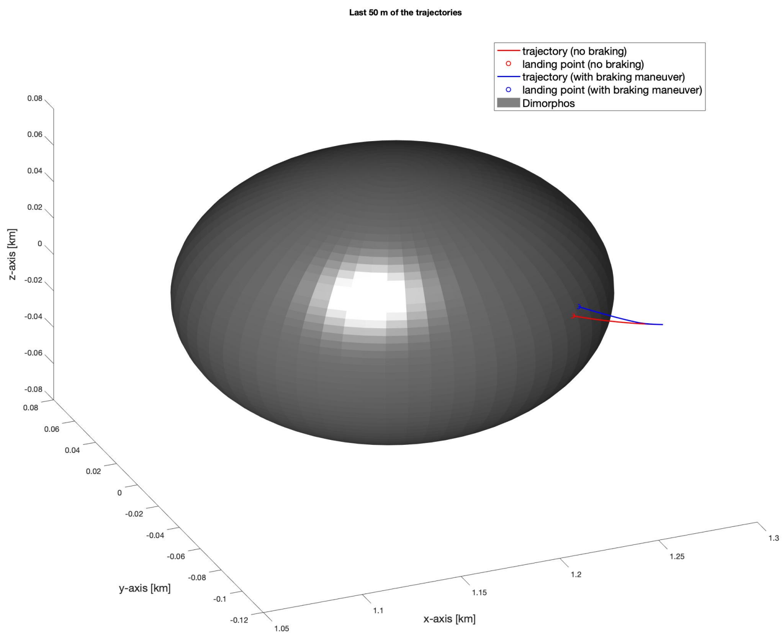

Figure 5.6: Last 50m of trajectories with and without braking maneuver in synodic frame.

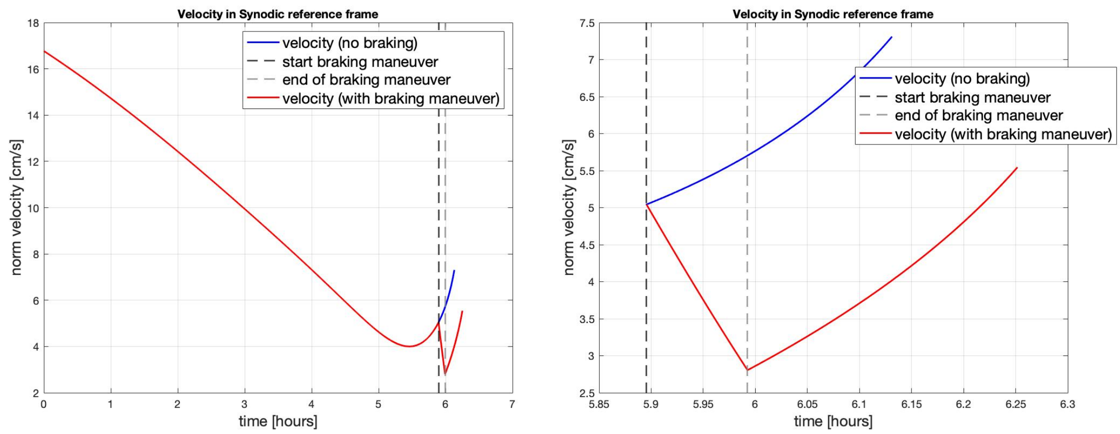

(a) Norm of the velocity. (b) Velocity after the braking maneuver.

Figure 5.7: Velocity in synodic frame.

velocity is 2cm/s, the total deltaV of the braking maneuver is 3.0588 cm/s. For time steps of 15 seconds, the maximum deltaV that can be computed respecting the constraint of the thrusters (1mN) and the mass of Juventas (12kg) is 0.1265 cm/s. In this example, the braking maneuver lasted 6 minutes. There is a total of 24 maneuvers applied at each time step with a maximum deltaV of 0.1265 cm/s.

The second scenario where 100 samples of trajectories are considered when the dispersion (see table 5.4 for 1-σ knowledge) on the position and velocity is performed at 50m, before the braking maneuver. Figure 5.8 shows the propagated trajectories after dispersion. In this example, every sample have impacted Dimorphos.

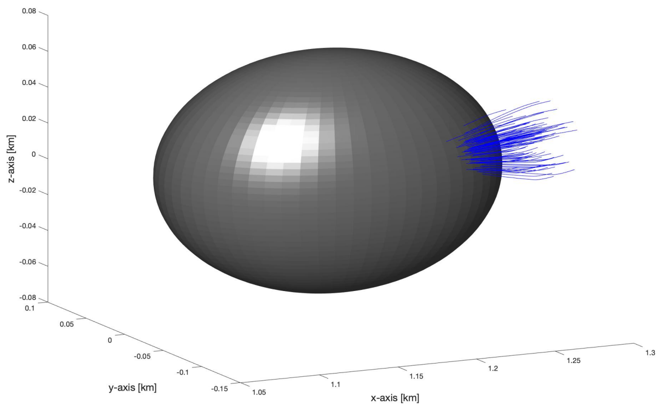

Figure 5.8: 100 samples of trajectories after dispersion.

The velocity during the descent is shown in Figure 5.9a and the impact velocity is summarized in the histogram from Figure 5.9b.

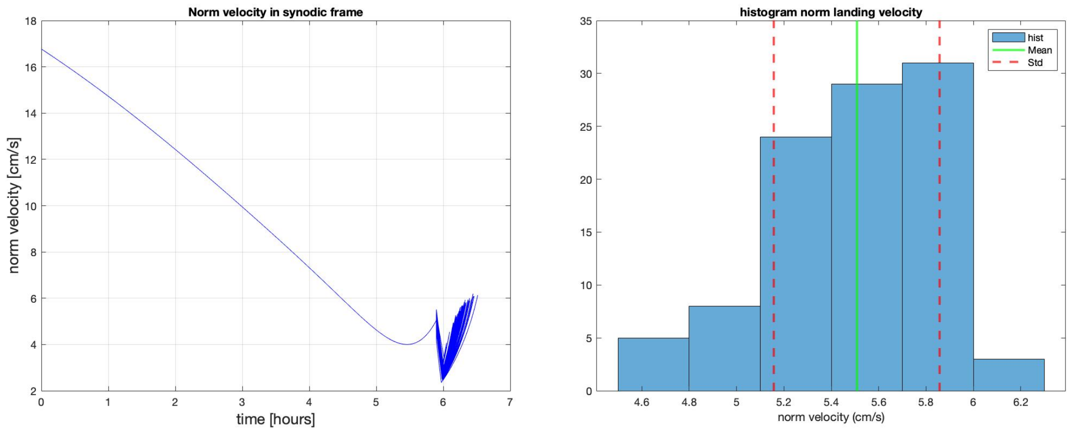

(a) Norm of the velocities. (b) Histogram of landing velocities.

Figure 5.9: Velocity in synodic frame for 100 samples.

The mean impact velocity is at 5.5082 cm/s with a standard deviation of 0.3500 cm/s. The average duration of the braking maneuver is 6.06 minutes.

It can be seen in Figure 5.9a that the velocity never reached the target of 2 cm/s. Indeed, the direction of the maneuver has been computed once at 50 m. During the descent, the instantaneous deltaV is applied in the same direction than the direction computed at 50m, meaning that the direction might have changed but is not considered in the model.

To have more precise results, a deeper Monte Carlo analysis will be done in the next chapter on more samples.

5.4 Shape models

Until now, Dimorphos was considered as a triaxial ellipsoid with a smooth surface (smooth ellipsoid model). This model is simplistic but still a good approximation of the current shape and is useful to perform preliminary studies. So having a numerical tool allowing to consider any arbitrary shape of Dimorphos would be of great interest as this thesis aims at having a more realistic model of Juventas in the Didymos system.

In this context, shape models are introduced. They are composed of vertices forming a surface mesh of triangles (called facets) when linked together and can represent any asteroid shape. It is defined so the normal of each triangle points outside the body.

The current shape of Dimorphos is unknown, but existing shape models from other known asteroids can be used. In this thesis, two shape models will be used. The first one is a simple ellipsoid shape model that will be useful for testing and comparing the results with the current smooth ellipsoid model. The second shape model is the Itokawa shape model. 25143 Itokawa is a near Earth asteroid that was the target of the Hayabusa spacecraft. Hayabusa landed in September 2005 and its surface was analysed and some samples were collected and returned to Earth [19]. During the mission, its shape has been computed and is widely used in celestial mechanics when the shape of asteroids is unknown. The shape model of Itokawa was derived by Robert Gaskell from Hayabusa images [24].

The ellipsoidal shape model is represented in Figure 5.10 and is available on DART's website [6]. It is composed of 1538 vertices and 3072 facets

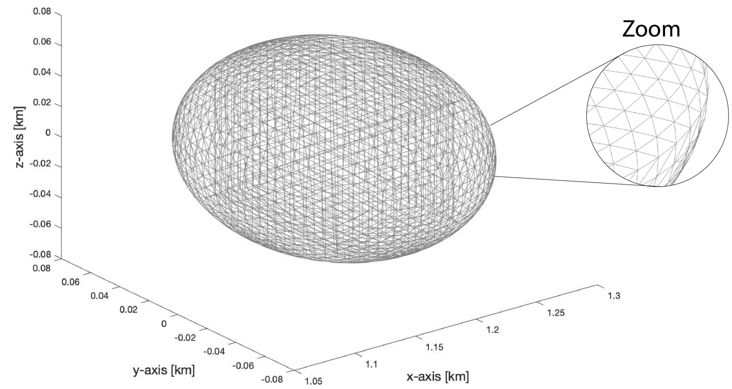

Figure 5.10: Ellipsoid shape model in synodic frame.

The Itokawa shape model is shown in Figure 5.11 and was provided by GMV. It is of higher resolution and composed of 98 306 vertices and 196 608 facets.

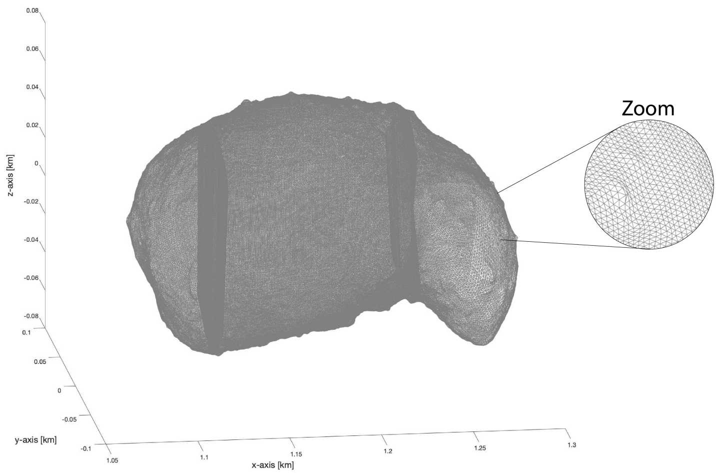

Figure 5.11: Itokawa shape model in synodic frame

In Appendix B, shape models are explained in more details and the computation of normals and centers of facets are derived.

5.4.1 Landing on shape models

In order to develop a bouncing model on an arbitrary shape model, finding the facet of landing is necessary as it will give the local normal needed for bouncing. Therefore, a numerical tool is developed here to find on which triangle the spacecraft lands.

The implementation is based on the use of event functions in Matlab. In Matlab, event functions [21] can stop the integration when a condition is reached. The idea is to stop the integration when the spacecraft is close to the shape model. Then, a facet will be selected and a second integration will be performed until landing on this facet. The selection is made by taking the facet that is the closest to the spacecraft in term of euclidean distance.

The event function uses the distance between the spacecraft and the vertices of the shape model as reference. However, computing the distance from the spacecraft to each vertices of the shape model is very expensive and the computational time increases with the resolution of the shape model. To solve this problem, the distance to the ellipsoid is used during the descent until the spacecraft gets close to the shape model. The distance d to an ellipsoid can be easily computed by

$$k_1 = \left\| \frac{\boldsymbol{r}_{moon}}{P} \right\| \tag{5.6}$$

$$k_2 = \left\| \frac{\boldsymbol{r}_{moon}}{P^2} \right\| \tag{5.7}$$

$$\rightarrow d = k_1 \frac{k_1 - 1}{k_2} \tag{5.8}$$

where $\boldsymbol{r}_{moon}$ is a three dimensional vector containing the position of the spacecraft relative to the center of Dimorphos and P is a three dimensional vector containing the semi principal axes (x_r, y_r, z_r).

Then, the distance between the spacecraft and each vertex is computed until a certain threshold is reached and the integration is stopped. Since the facets have different sizes, the threshold will be chosen as half the maximum distance between two vertices in each facet.

Finally, when reaching this threshold, the closest facet to the spacecraft is selected and a new integration with small time steps of 1 s is performed. The scalar product between the normal of the facet and the vector composed of a vertex and the spacecraft is computed at each iteration. If the scalar product changes sign, it means that the spacecraft has crossed the facet and is inside the body and thus the integration is stopped. With this method, the landing point on the facet is very precise because the time steps are very small.

The algorithm developed is summarized here :

1. The distance between the spacecraft and the ellipsoid is computed at each iteration until the spacecraft is close to the desired shape model. Then, the distance between the spacecraft and the shape model is computed at each iteration until a threshold is reached and the integration is stopped.

2. The closest facet to this point is selected.

3. A new integration is performed with small time steps until the selected facet is crossed. The integration is stopped and the spacecraft has impacted the facet.

The algorithm developed is now performed for the nominal trajectory on the ellipsoid shape model as shown on Figure 5.12 and the Itokawa shape models, see Figure 5.13

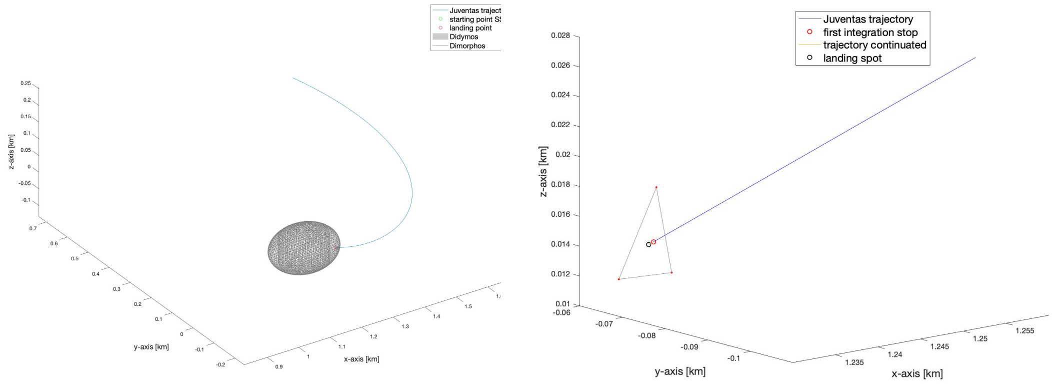

(a) Landing on ellipsoid shape model.

(b) Landing on the selected facet.

Figure 5.12: Nominal trajectory landing ellipsoid shape model.

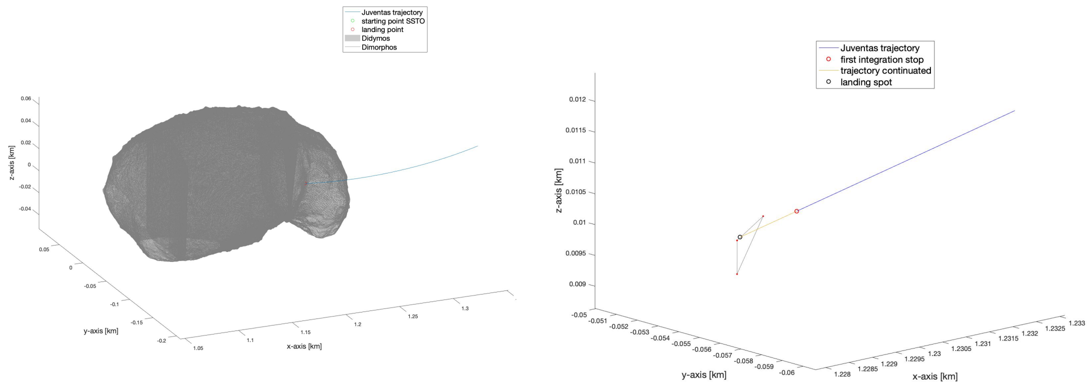

(a) Landing on Itokawa shape model.

(b) Landing on the selected facet.

Figure 5.13: Nominal trajectory landing Itokawa shape model.

5.5 Bouncing

After the spacecraft has impacted Dimorphos, the final part of the mission can begin as Juventas will bounce on the surface of Dimorphos. Modelling the interactions and collisions between the spacecraft and the surface can be a tedious task and very unpredictable. In this section, a simplistic bouncing model is presented. Having a simplistic model that is fast and reliable will be useful when performing Monte Carlo simulations in the next chapter where many trajectories will be computed.

In this thesis, the spacecraft is considered as a point. Thus a point mass bouncing model will be implemented for the different models of Dimorphos.

5.5.1 Bouncing model

In this model, the impact is purely cinematic as it involves the velocity of the spacecraft. A coefficient of restitution is introduced and represents the amount of energy kept during the collision on the surface. The coefficient of restitution is the ratio between the final and initial velocity of the spacecraft when colliding with the surface and shall range between 0 and 1 where 0 would be a perfectly inelastic collision and 1 a perfectly elastic collision [28]. On the asteroid surface, very elastic shocks should be expected when impacting the surface as the velocities are very small. However, the surface could have material that could significantly reduce the energy of a bounce [27].

The spacecraft impacts the surface with a velocity that has a specific direction and magnitude. The velocity can be decomposed in its tangential and normal components, see Figure 5.14.

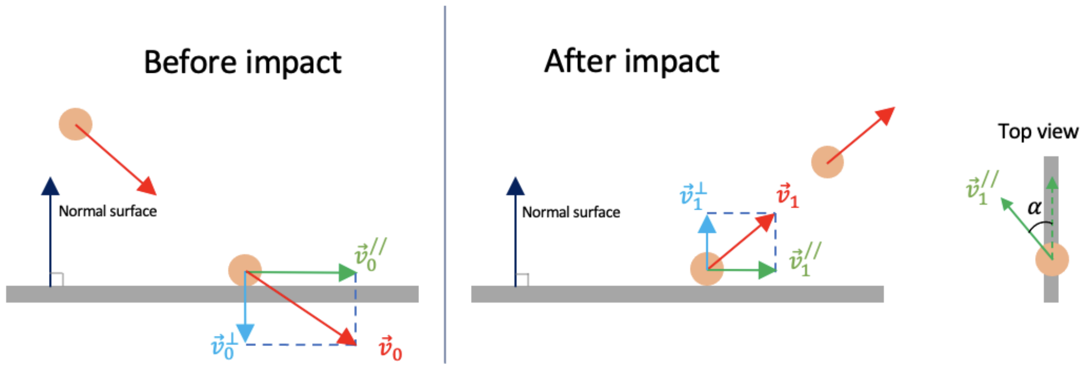

Figure 5.14: Velocity decomposition at impact.

The physical interaction between the spacecraft and the surface is described by two coefficients of restitution: the coefficient of the normal velocity, e and the coefficient of the tangential velocity, f. They are defined as

$$e = \frac{v_1^{\perp}}{v_0^{\perp}}, \quad f = \frac{v_1^{\parallel}}{v_0^{\parallel}}$$

The normal coefficient of restitution has value ranging from 0 to 1. The tangential coefficient of restitution can have negative value as there could be bounces in the opposite direction and has value ranging from -1 to 1.

The coefficient of restitution e is estimated using results from previous studies. The first estimate is based on the observation of the near-Earth asteroid 25143 Itokawa where the spacecraft Hayabusa bounced with a coefficient of restitution of approximately 0.8 [33]. On the other hand, the observations of the landing by the spacecraft NEAR-Shoemaker on asteroid 433 Eros gave a coefficient of restitution of approximately 0.1 [7]. These two estimations gives a good range of values for the coefficient e and will be considered as two extreme cases in our analysis.

e and f should be related physically. If e is small, f should also be small. It would be hard to justify physically having a e of 0.1 and a f of 0.8. In this thesis, e and f will be considered equal but f could be negative.

To make the bouncing model more realistic and model the orientation of the spacecraft when impacting the surface, randomness is added to the direction of the tangential velocity. This will give bounces in different directions. A new parameter α is added , see Figure 5.14 and defined as

$$\alpha \in [-45°, 45°]$$

With the new parameter α, randomness is added at each bounce. α is chosen randomly following a normal distribution.

In this model, as long as $e > 0$ and $f > 0$, the spacecraft will experience an infinite number of bounces. Thus, defining stopping conditions on the bouncing are needed. The number of maximum bounces allowed is 50. In the case of the smooth ellipsoid model and ellipsoid shape model, velocities below 1mm/s and a last bounce with maximum height of 50cm will stop the simulation. In the case of the Itokawa shape model, a stopping condition on the normal velocity of 1mm/s is defined and on the size of the bounce, i.e if the bounce is less than the size of a facet of approximately 1m, is considered.

5.5.2 Implementation and results

The bouncing model developed can now be implemented on the different models of Dimorphos : the smooth ellipsoid, the ellipsoid shape model and the Itokawa shape model.

At impact, the local normal of the surface is computed. On the smooth ellipsoid model, the local normal can be computed using the gradient of the surface of a triaxial ellipsoid. For shape models, the spacecraft lands on a facet as derived in the previous section and thus the normal of this facet is computed as described in Appendix B.

Now having the local normal of the surface, the velocity vector can be decomposed into tangential and normal components. The resulting outgoing velocity is computed when multiplying by the coefficient e and f respectively.

The bouncing model is implemented on the nominal trajectory for different values of e and f for each model : $e = [0.1, 0.3, 0.6, 0.8]$ and $f = [0.1, 0.3, 0.6, 0.8]$.

For the smooth ellipsoid model, the corresponding nominal trajectory with the bouncing is shown on Figure 5.15.

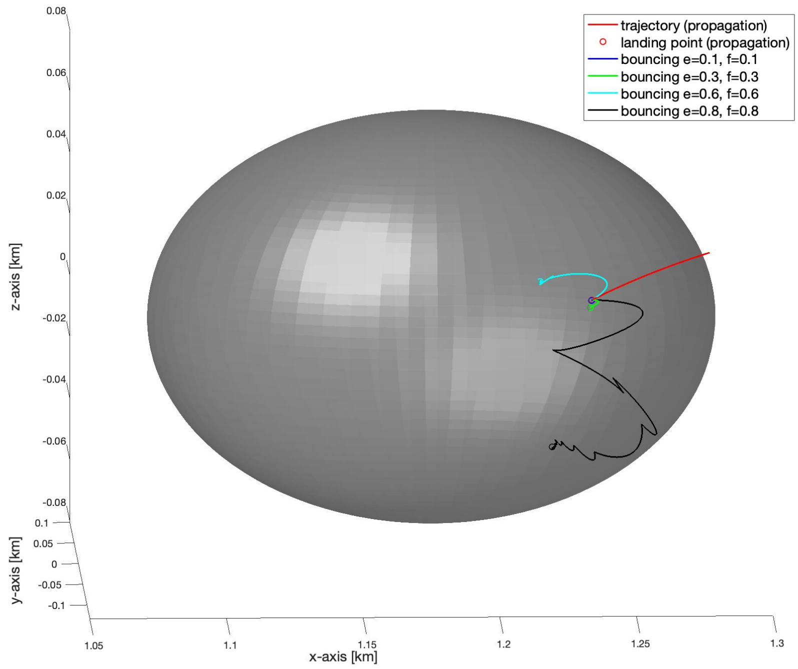

Figure 5.15: Bouncing on the smooth ellipsoid model in synodic frame.

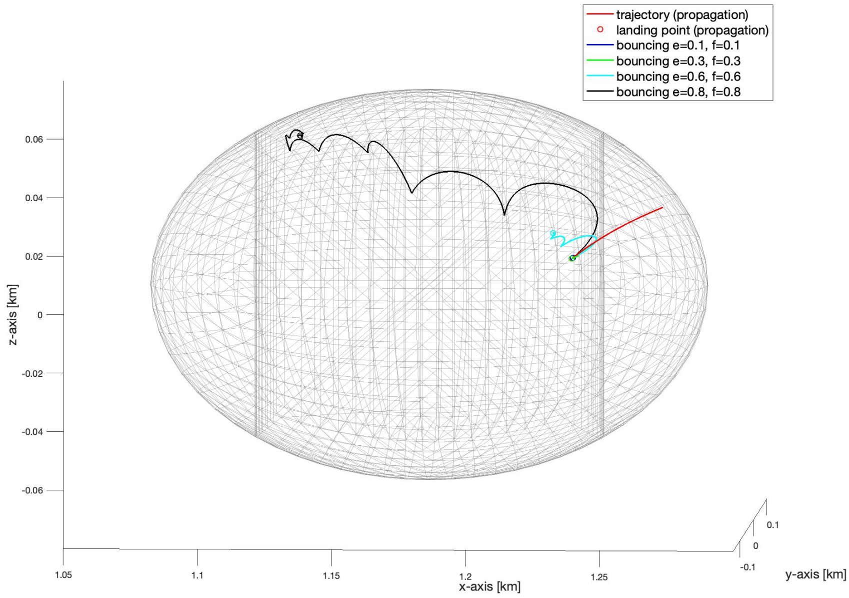

Figure 5.16: Bouncing on the ellipsoid shape model in synodic frame.

The same results are shown on Figure 5.16 for the ellipsoid shape model.

The height of the bounces through time for both ellipsoid model are shown in Figure 5.17

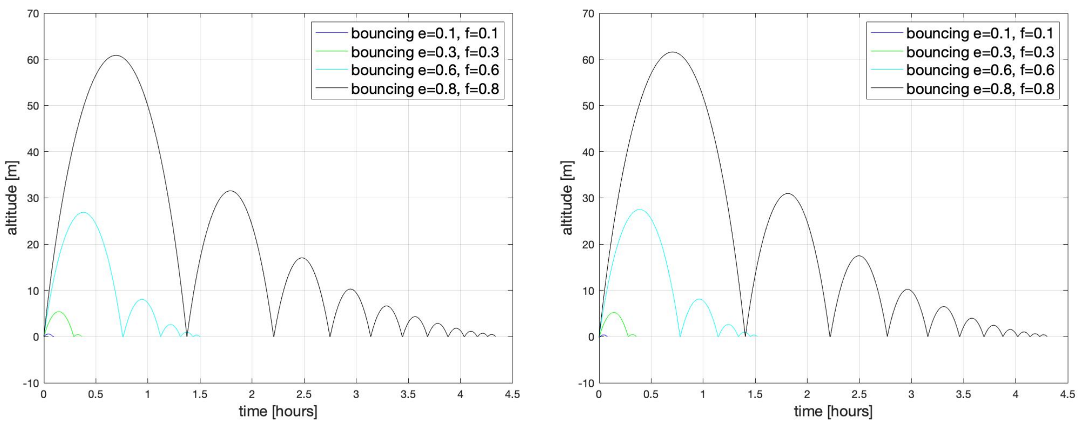

(a) Smooth ellipsoid model. (b) Ellipsoid shape model.

Figure 5.17: Height of bounces as a function of time for both ellipsoid model.

Finally, the bouncing is implemented on the Itokawa shape model and is shown on Figure 5.18. On a arbitrary shape model such as Itokawa, computing the height of a bounce is not possible and will then not be shown here.

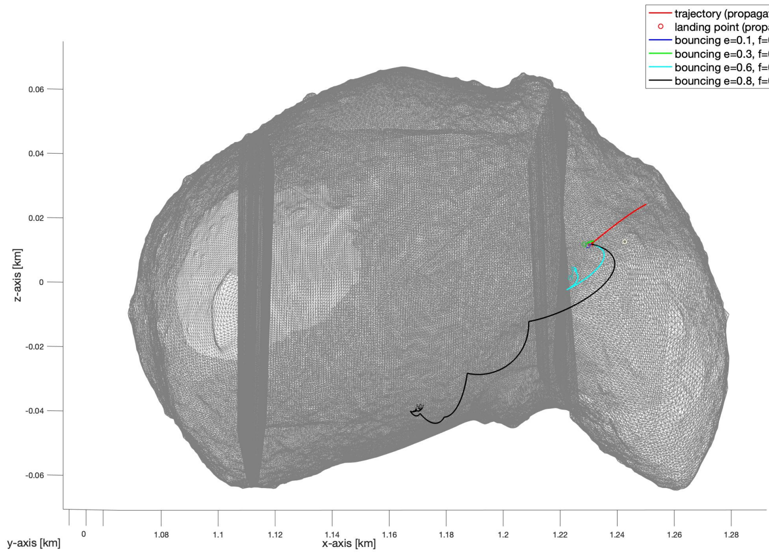

Figure 5.18: Bouncing on the Itokawa shape model

The results for each Dimorphos model are summarized in table 5.5. It can be seen that the restitution coefficients have a very important effect on the bouncing. Each model gives similar results. It should be expected for the two ellipsoid models as they represent the same shape. However, the number of bounces and the duration of bouncing is also consistent with the Itokawa shape model. It can be concluded that the bouncing model implemented is working and the results are coherent and could represent real bouncing effects.

The influence of bouncing parameters on the bouncing will be studied in the next chapter using Monte Carlo analyses.

Restitution coefficients	Data	Smooth ellipsoid model	Ellipsoid shape model	Itokawa shape model
$e = 0.1$, $f = 0.1$	nbr bounces	1	1	1
	Highest bounce [m]	0.5629	0.3652	N/A
	Duration bouncing [h]	0.0987	0.0788	0.0958
$e = 0.3$, $f = 0.3$	nbr bounces	2	2	3
	Highest bounce [m]	5.4140	5.2625	N/A
	Duration bouncing [h]	0.3653	0.3603	0.2993
$e = 0.6$, $f = 0.6$	nbr bounces	5	5	5
	Highest bounce [m]	26.8871	27.3402	N/A
	Duration bouncing [h]	1.4996	1.5146	1.0167
$e = 0.8$, $f = 0.8$	nbr bounces	11	11	13
	Highest bounce [m]	60.8488	61.8946	N/A
	Duration bouncing [h]	4.3382	4.3776	4.5155

Table 5.5: Summary bouncing on nominal trajectory

Chapter 6

Monte Carlo analysis

In Chapter 5, a brief introduction to the study of the uncertainties of the nominal trajectories was introduced. Dispersion on the position and velocity before the braking maneuver was considered. The influence of the coefficients of restitution on the bouncing was also studied for different Dimorphos models. In this Chapter, a complete Monte Carlo analysis is performed to assess the robustness of the landing trajectory with and without braking maneuver.

6.1 Preliminaries

The uncertainties considered for the Monte Carlo analysis are first presented. Then, the parameters that will be analyzed are identified and described. Finally a convergence analysis is performed to study the number of samples needed for the Monte Carlo simulations.

As seen in Chapter 5, the behavior of the bouncing is relatively equivalent for each Dimorphos models. For simplicity's sake, the Monte Carlo analysis will only be considered for the smooth ellipsoid model. The conclusion drawn in this Chapter can be extrapolated for the other models.

6.1.1 Uncertainties

Two sources of uncertainties are considered for the Monte Carlo analysis : the uncertainties related to the GNC and the uncertainties related to the Didymos system.

As Described in Chapter 5.1, the 1-σ uncertainties on the position and velocity at

50m in inertial frame, before the braking maneuver were given by GMV and are summarized in Table 6.1.

Parameters	**1-σ uncertainty**	**Unit**
Position		
X; Y; Z	11.54; 9.04 ; 9.25	m
Velocity		
X; Y; Z	2.46; 1.22 ; 1.14	mm/s

Table 6.1: Uncertainties from the GNC.

The main source of uncertainty from the Didymos system is the total mass as it is currently not a well known quantity. The uncertainty on the total mass is suggested to be approximately 10% of the nominal value as described in Table 6.2 as proposed by GMV and the ROB.

Parameters	**Value**	**Unit**
Total mass	$5.4114e^{11} \pm 0.5411e^{11}$	kg

Table 6.2: Uncertainty of the Didymos system.

6.1.2 Monte Carlo parameters

To study and characterize the landing trajectories, many relevant information can be drawn at impact and during the bouncing. The following parameters are introduced :

- Success rate : the percentage of trajectories staying on Dimorphos after impact and not bouncing off.
- Impact velocity.
- Latitude and Longitude at impact.
- Number of bounces.
- Height of the first bounce.
- Duration of bouncing.

6.1.3 Convergence

The number of samples needed in the Monte Carlo simulation is studied through a convergence analysis. The convergence analysis is performed using sensitive parameters where the the behavior of the trajectories would be the most uncertain. That is for the extreme cases on the mass of -10% and both coefficients of restitution of 0.8. This lead to the worst case scenario where many trajectories are expected to bounce off the attraction of Dimorphos after impact.

The following parameters are studied : the impact velocity, the success rate, the latitude and longitude at impact and the number of bounces. The results are shown in Figure 6.1 for a total of 5000 samples.

From Figures 6.1a, 6.1b, 6.1c, 6.1d approximately between 1500 and 2000 samples are needed to assure convergence. The number of bounces is computed with only the trajectories that have landed on Dimorphos and that did not bounce off. It can be seen in Figure 6.1e that 500 samples are needed which would result to 2000 samples of the total simulations.

Finally, the number of samples chosen for the Monte Carlo analysis is 2000 as it assure convergences of the quantities in the worst case scenario.

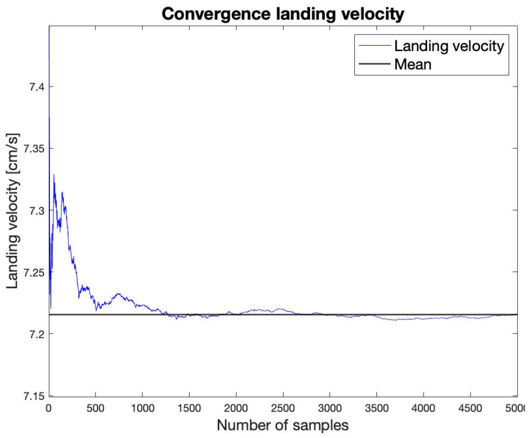

(a) Mean impact velocity.

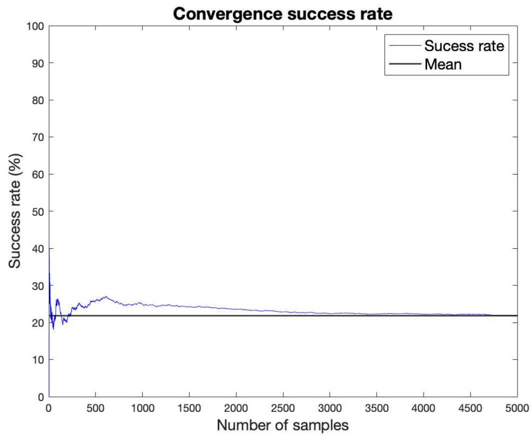

(b) Success rate.

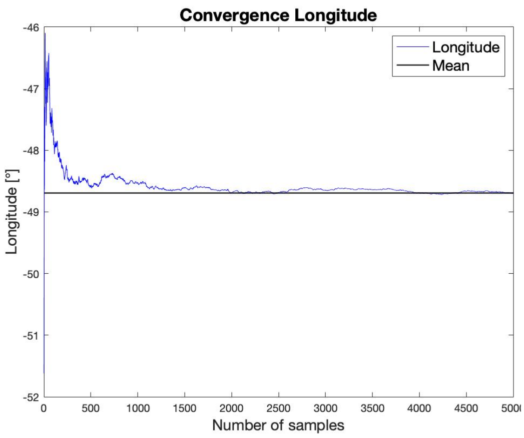

(c) Mean longitude at impact.

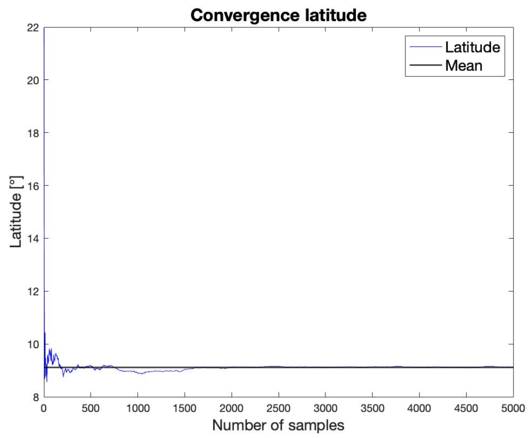

(d) Mean latitude at impact.

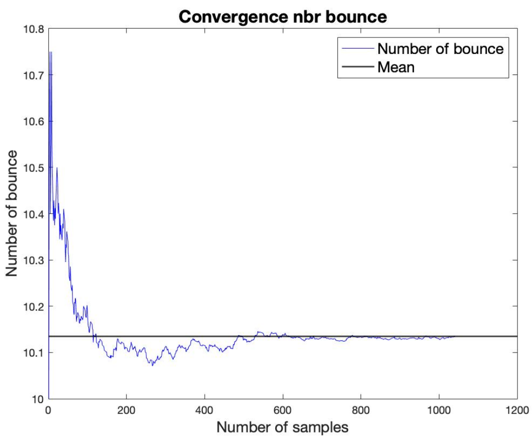

(e) Mean number of bounces.

Figure 6.1: Convergence for 5000 samples.

6.2 Nominal mass and randomized coefficients of restitution

The first set of simulations are performed considering the dispersion on the position and velocity at 50m. The nominal value of the mass is kept and the coefficients of restitution are uniformly distributed. As a reminder, the normal coefficient of restitution, e ranges between 0.1 and 0.8 and the tangential coefficient of restitution, f ranges between -0.8 and 0.8.

The distribution of the Monte Carlo parameters are studied for 2000 samples of landing trajectories with and without braking maneuver. The mean and 1-σ are also used to support the analysis.

6.2.1 Results at impact

The distributions of the impact velocity is shown in Figure 6.2. The impact velocity can go up to 8.3 cm/s without the braking maneuver and 6.3 cm/s with the braking maneuver. On average, the mean impact velocity is 7.3038 cm/s without braking maneuver and 5.4355 cm/s with braking maneuver (see Table 6.3). This gives a difference of 1.8683 cm/s between them. The braking maneuver reduces the impact velocity of almost 2 cm/s on average. The 1-σ values are relatively small so the majority of the trajectories are spread around the mean values. Low variations of the impact velocity is expected.

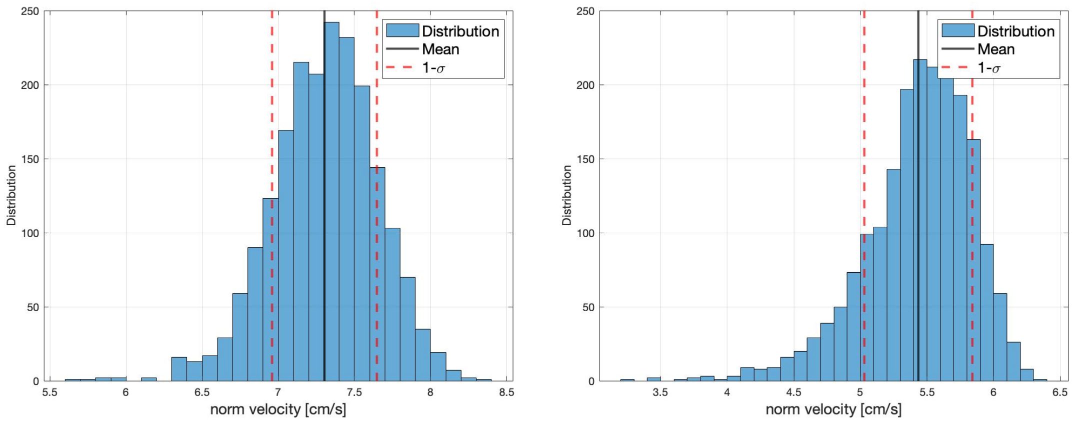

(a) Without braking maneuver. (b) With braking maneuver.

Figure 6.2: Histogram impact velocity.

Trajectories	Mean impact velocity	1-σ impact velocity
Without braking maneuver	7.3038 cm/s	0.3448 cm/s
With braking maneuver	5.4355 cm/s	0.4057 cm/s

Table 6.3: Summary impact velocity.

The landing sites are now studied where the distributions of the latitude and longitude at impact are shown in Figure 6.3 with and without braking maneuver and summarized in Table 6.4. A difference of 4.2642° in Longitude and 1.2593° in Latitude can be expected between them. The landing sites on Dimorphos are similar and the effect of the braking maneuver is relatively low.

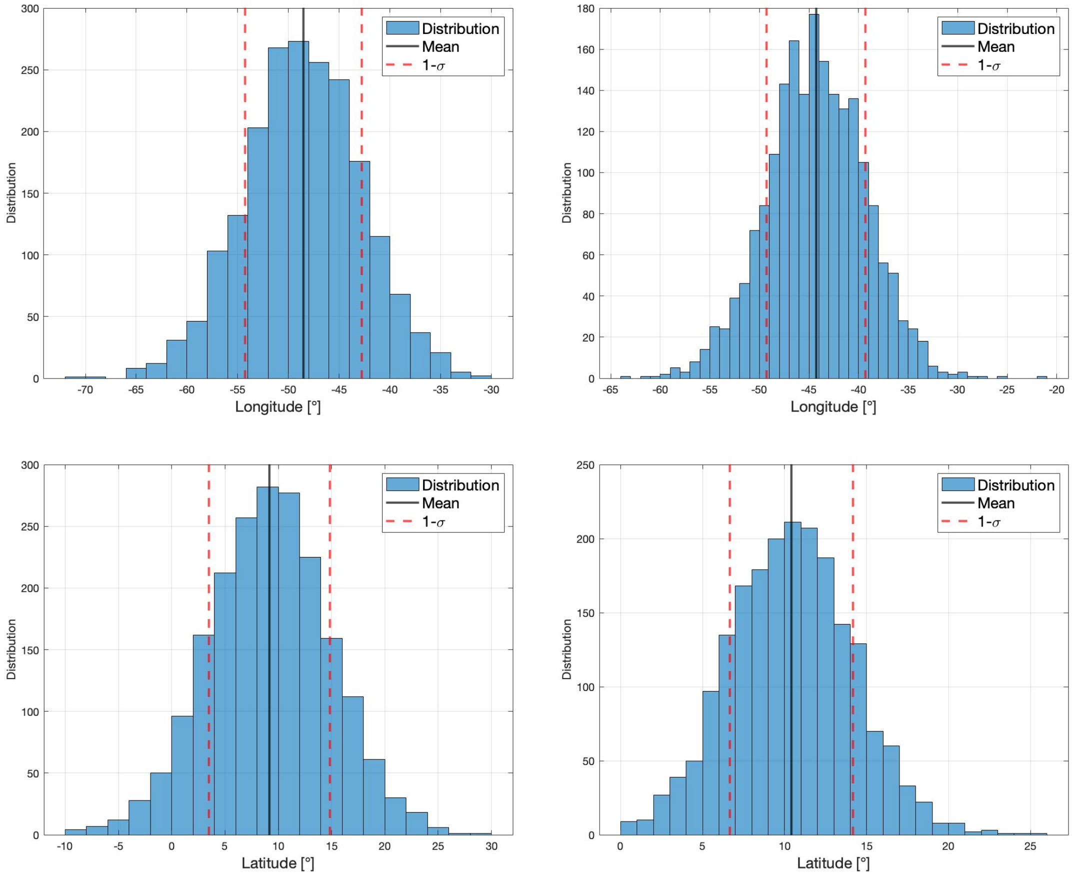

(a) Without braking maneuver. (b) With braking maneuver.

Figure 6.3: Histogram Latitude and Longitude at impact.

Trajectories	Mean impact Longitude	1-σ Longitude	Mean impact Latitude	1-σ Latitude
Without braking maneuver	-48.5470°	5.7458°	9.1544°	5.6643°
With braking maneuver	-44.2828°	4.9896°	10.4137°	3.7450°

Table 6.4: Summary Latitude and Longitude at impact.

6.2.2 Results bouncing

For the analysis of the bouncing, three quantities are studied : the number of bounces, the height of the first bounce and the duration of bouncing. Their distributions with and without braking maneuver is shown in Figure 6.4 and summarized in Table 6.5.

As it can be seen the bouncing is very unpredictable and high variation in these three quantities are expected. For instance, the number of bounce is between 2 and 10 bounces without braking maneuver and between 1 and 9 bounces with braking maneuver. Overall, one less bounce is expected with the braking maneuver. The height of the first bounce can go as high as 70 m without braking maneuver and 30 m with braking maneuver which lower the chance of bouncing off Dimorphos. However, the standard deviation of the height is very high of the order of the mean value which can lead to very high variations. The same conclusion can be drawn for the duration of bouncing where the braking maneuver has a similar impact. Indeed, the duration can be as high as 4.5 h without braking maneuver and 3 hours with braking maneuver and very high variation can also be expected between for the mean values.

The general trend is that lower impact velocity leads to lower number of bounces, lower height of first bounce and lower duration of bouncing. It is important to note that minimizing these three quantities is essential for the mission's success. Indeed, having fewer and lower bounces would limit the overall damage on the spacecraft during bouncing. Lower duration of bouncing would limit battery consumption during the bouncing which would lead to having enough battery left for surface analysis once the spacecraft is at rest on the surface.

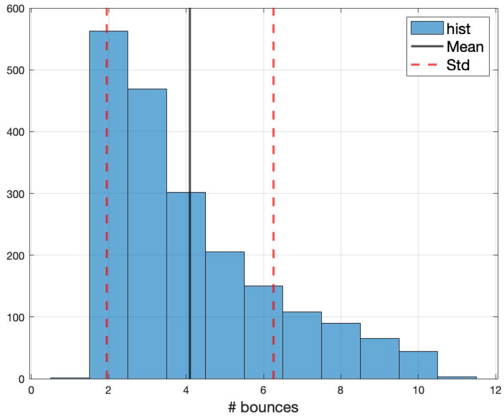

(a) Without braking maneuver.

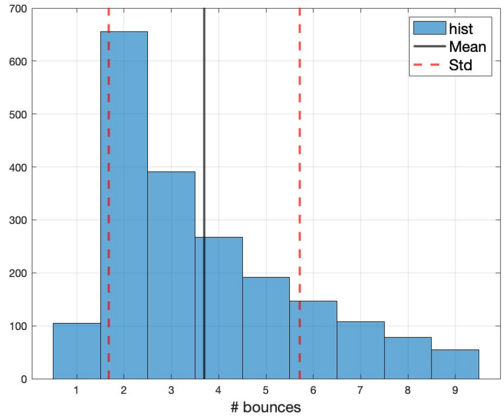

(b) With braking maneuver.

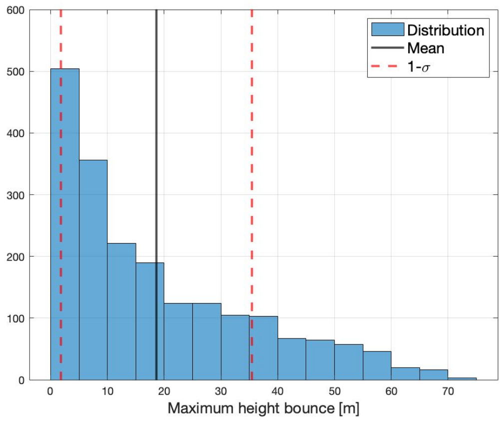

(c) Without braking maneuver.

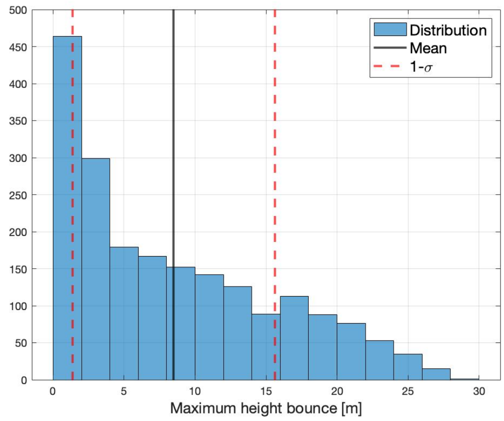

(d) With braking maneuver.

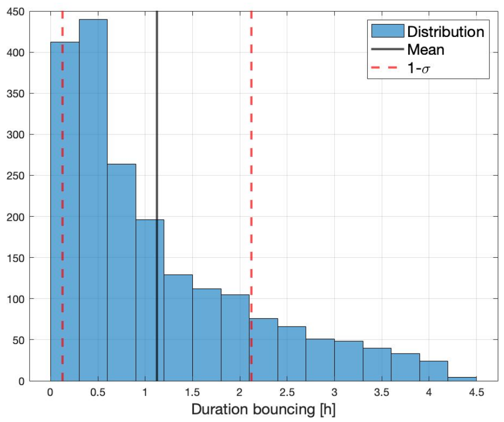

(e) Without braking maneuver.

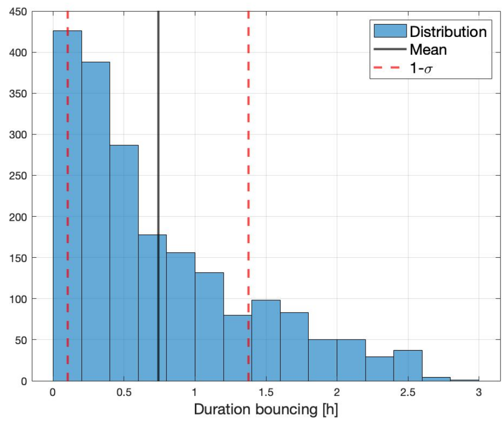

(f) With braking maneuver.

Figure 6.4: Histogram bouncing.

Without braking maneuver		
Parameters	Mean value	1-σ value
Number of bounces	4.1005	2.1549
Height first bounce	18.66165 m	16.8330 m
Duration bouncing	1.1230 h	0.9966 h
With braking maneuver		
Parameters	Mean value	1-σ value
Number of bounces	3.6893	2.0187
Height first bounce	8.49567 m	7.1169 m
Duration bouncing	0.7398 h	0.6357 h

Table 6.5: Summary bouncing.

Finally, the landing sites at impact and after bouncing (at rest) are shown in Figure 6.5. It can be seen that the landing sites after bouncing are more widely spaced without braking maneuver as bigger and longer bounces are expected. The landing sites are thus more concentrated to its initial position with braking maneuver.

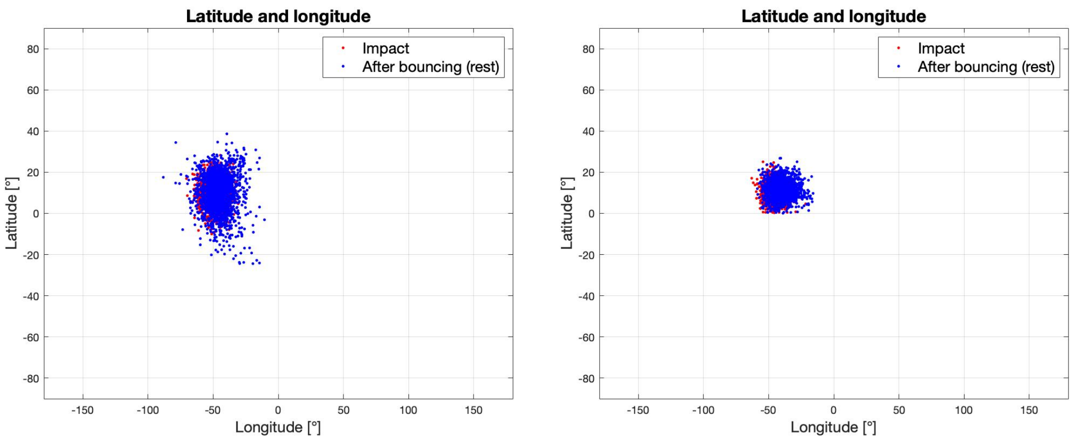

(a) Without braking maneuver. (b) With braking maneuver.

Figure 6.5: Landing sites at impact and after bouncing.

6.3 Nominal mass and extreme coefficients of restitution on the bouncing

From section 6.2, the results showed that bouncing is very unpredictable and high variations occur when the coefficients of restitution are randomized. It would be of interest to study the bouncing with extreme cases of these coefficients to have an idea of the expected general trend of the effect of the maximal and minimal coefficients of restitution have for the behavior of the bouncing on the surface of Dimorphos.

In this section, the two following cases are considered :

- maximum coefficients of restitution : $e = 0.8,\ f = 0.8$
- minimal coefficients of restitution : $e = 0.1,\ f = 0.1$

6.3.1 Results for $e = 0.8,\ f = 0.8$

The first important observation is the success rate, defined as the percentage of trajectories that did not bounce off Dimorphos after impact. The success rate is 86% without braking maneuver and 99.85% with braking maneuver (see Table 6.6) . Here the effect of the braking maneuver on the mission success is crucial as almost all trajectories have landed and not bounced off Dimorphos.

Parameters	Without braking maneuver	With braking maneuver
Success rate	86 %	99.85 %

Table 6.6: Success rate for $e = 0.8,\ f = 0.8$.

The three bouncing parameters to analyze are shown in Figure 6.6 and the mean and 1-σ values are summarized in Table 6.7. The distribution are much more consistent and little variation are expected than seen previously in section 6.2. The number of bounces is between 9 to 13 without braking maneuver and ranging between 8 to 12 with braking maneuver. The mean number of bounces is 11.4888 without braking maneuver and 9.7436 so approximately a difference of two bounces between them is expected. The 1-σ values are relatively low so the results are concentrated around the mean values. The height of the first bounce is on average more than two times higher without a braking maneuver. Finally, the duration of bouncing is on average less than two times lower with a braking maneuver. Overall, the behavior of the bouncing is as expected and the effect of the braking maneuver is very important.

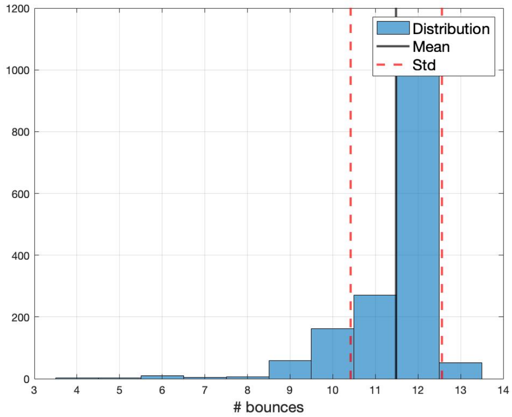

(a) Without braking maneuver.

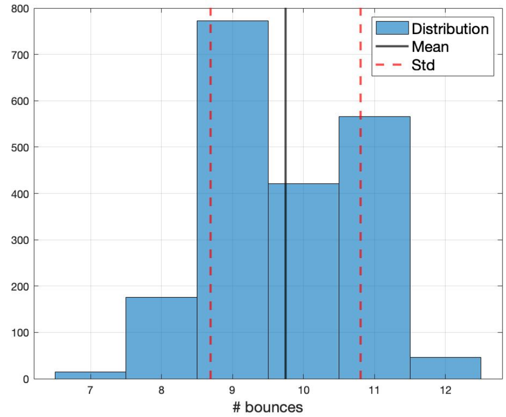

(b) With braking maneuver.

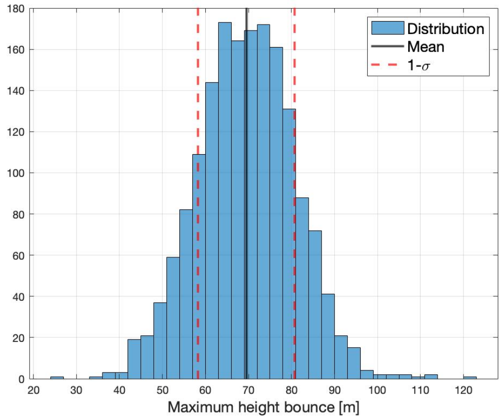

(c) Without braking maneuver.

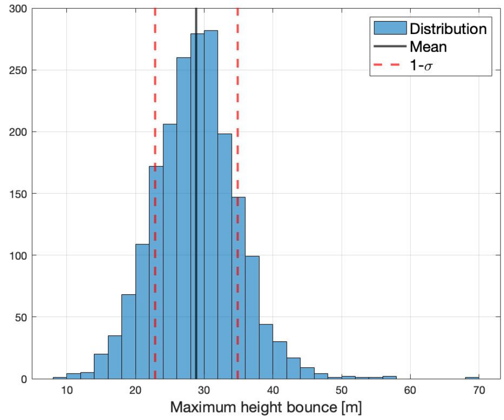

(d) With braking maneuver.

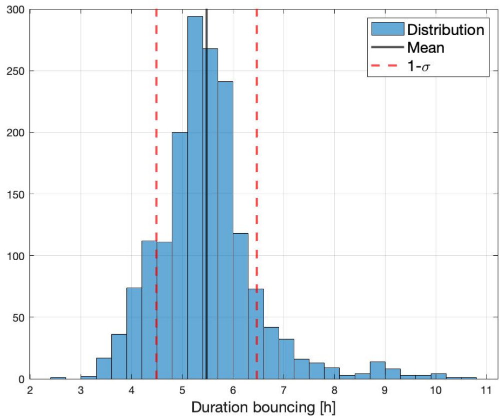

(e) Without braking maneuver.

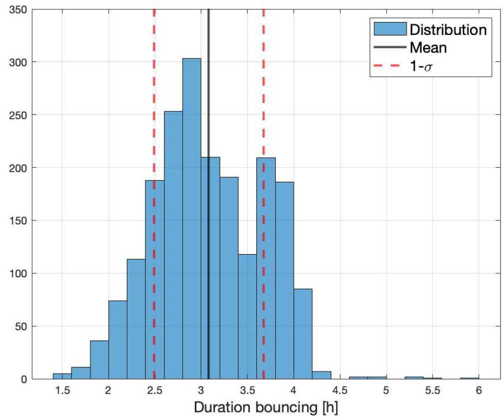

(f) With braking maneuver.

Figure 6.6: Histogram bouncing for $e = 0.8,\ f = 0.8$.

Without braking maneuver		
Parameters	Mean value	1-σ value
Number of bounces	11.4888	1.0715
Height first bounce	69.49117 m	11.2783 m
Duration bouncing	5.4776 h	0.9913 h
With braking maneuver		
Parameters	Mean value	1-σ value
Number of bounces	9.7436	1.0572
Height first bounce	28.85627 m	6.0284 m
Duration bouncing	3.0817 h	0.5906 h

Table 6.7: Summary bouncing for $e = 0.8,\ f = 0.8$.

The landing sites dispersion is shown in Figure 6.7. They make a nice flock of points with braking maneuver while they are more spread out without braking maneuver.

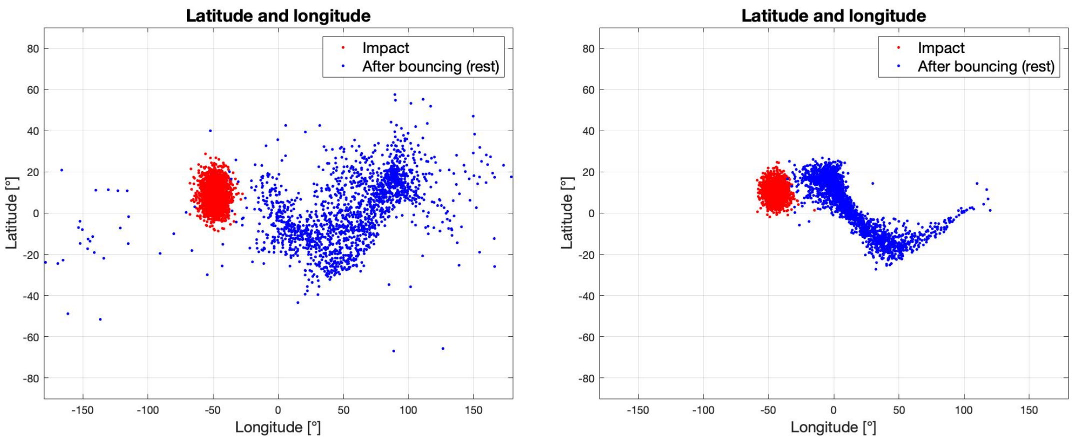

(a) Without braking maneuver. (b) With braking maneuver.

Figure 6.7: Landing sites at impact and after bouncing for $e = 0.8,\ f = 0.8$.

6.3.2 Results for $e = 0.1,\ f = 0.1$

The bouncing for the coefficients $e = 0.1,\ f = 0.1$ is not very interesting and redundant. The distribution of the parameters are shown in Appendix C if the reader is interested. The behavior is the same, with such low coefficients, no trajectory bounces off Dimorphos and the bounces are very small : between 1 and 2 bounces can be expected without braking maneuver while only one bounce occurred with braking maneuver.

6.4 Sensitivity mass

Until now, the nominal mass was taken into consideration. In this section, at 50m the total mass is varied between -10% and 10% of its nominal value as follows :

Total mass $\times e^{11}$[kg]								
4.8703	5.0326	5.1409	5.2491	5.4114	5.5738	5.6820	5.7903	5.9526

The very interesting parameter to study for the dispersion on the mass is the success rate as a function the coefficients of restitution. Coefficients raging from 0.1 to 0.8 are studied. A heatmap of the success rate is shown with and without braking maneuver in Figure 6.8).

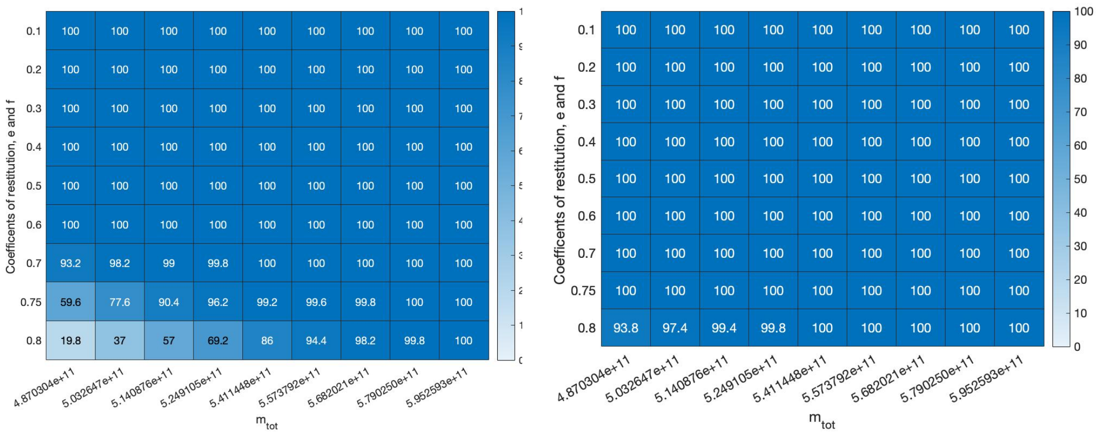

(a) Without braking maneuver.

(b) With braking maneuver.

Figure 6.8: Success rate varying the total mass and the coefficients of restitution.

As expected, the lower the mass, the less attraction will be felt on the spacecraft and the risk of bouncing off will be higher. Varying the total mass has an impact on the success rate but is dependent on the coefficients of restitution.

For instance, the extreme case for -10% of its nominal mass and for coefficients of restitution of 0.8 has a success rate of 19.2% without braking maneuver. Thanks to the braking maneuver, the success rate jumps to 93.8% in that case. It means that in the worst case, the braking maneuver would increase the success of the mission drastically as the success rate is much higher and the majority of trajectories have landed on Dimorphos.

In the case of +10% of the nominal mass, nothing is expected as the spacecraft would fall faster to Dimorphos which reduces the chance of bouncing off. Indeed, in Figure 6.9 the impact velocity is shown for the different values of the mass in the case of the braking maneuver and is summarized in Table 6.8. Varying the total mass yields a difference of the impact velocity of 0.1594 cm/s between the -10% and +10% case. This change in velocity is insignificant for the mission.

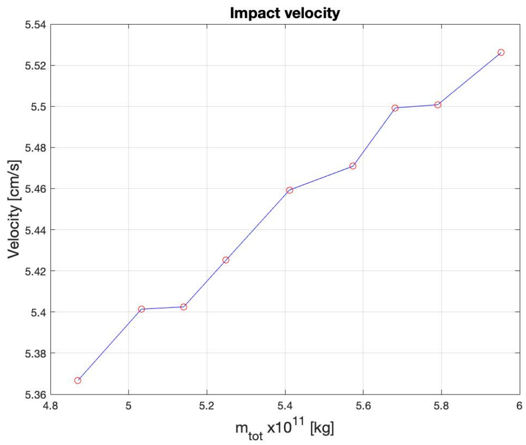

Figure 6.9: Impact velocity with braking maneuver.

Total mass $\times e^{11}$[kg]								
4.8703	5.0326	5.1409	5.2491	5.4114	5.5738	5.6820	5.7903	5.9526
Impact velocity [cm/s]								
5.3667	5.4014	5.4025	5.4252	5.4593	5.4709	5.4992	5.5008	5.5261

Table 6.8: Summary impact velocity with braking maneuver.

6.5 Discussions

In this Chapter, a Monte Carlo analysis was performed and some interesting results have been found. A general trend observed was the benefit of the braking maneuver for every Monte Carlo parameters considered due to the impact velocity being lower.

The effect of the braking maneuver can be summarized below :

- A diminution of approximately 2 cm/s was observed on the impact velocity.

- The chance of bouncing off Dimorphos is reduced drastically. Almost all trajectories have landed.
- The number of bounces was decreased by 1.
- The height of the bounce was more than halved.
- The duration of bouncing was almost halved.

Reducing the impact velocity increases the mission's success and should be considered of great importance to assure a safe landing of Juventas. Lower bounces would reduce the overall damage that could be caused to the spacecraft and its payload. Lower duration of bouncing would give more time for Juventas to make its surface analysis as its battery is limited.

Conclusion

This thesis can be divided in three main contributions. Firstly, the analysis of Vanhalst and Hanon (2020) to make the computation of landing trajectories faster using a vectorized numerical integrator. Secondly, the improvement of the model of the motion of the spacecraft in the Didymos system by adding a new orbital perturbation, a braking maneuver, shape models and a bouncing model. Finally, a Monte Carlo analysis of the landing trajectory was performed. The summaries of these contributions are presented below.

Vectorized integrator

The vectorized numerical integrator implemented was compared to simple loop-based *ode113* code and performs on average 20 to 30 times faster to solve initial value problems.

The newly vectorized integrator was added to the loop-based code that Vanhalst and Hanon(2020) used to compute and study landing trajectories. For the backward propagation containing 26,079 trajectories to compute, the loop-based code took 8 hours to run 26 epochs. Thanks to the vectorized integrator, the backward propagation takes 4.32 minutes which is 111 faster. Concerning the Monte Carlo simulations, more than 12.5 hours were required to compute 77,500 trajectories. With the vectorized integrator, the simulations took 4.65 minutes which is more than 161 times faster.

This vectorized numerical integrator could be used to perform further studies involving the computation of a huge set of landing trajectories. But it could also be used on other project requiring the use of an integrator to solve tens of thousands of initial value problems quickly. The scope of its use is wide and can reach various fields.

Landing trajectory model

A nominal landing trajectory was provided by GMV and the model of Juventas in the vicinity of Didymos was improved. First a new orbital perturbation for Dimorphos was considered and validated. A braking maneuver was added to the model to reduce the landing velocity and mimic the use of the GNC on board the Juventas spacecraft. Dimorphos was represented by shape models to make the model more realistic and a landing strategy was developed. The bouncing model was presented and implemented for the different shapes of Dimorphos.

Analysis of the uncertainties

To study the uncertainties related to GNC and the Didymos system, a Monte Carlo analysis was performed on the smooth ellipsoid model. The dispersion on the position and velocity at 50m was considered and different results varying the total mass and the coefficients of restitution were studied for trajectories with and without braking maneuver.

Concerning the impact, the landing velocity was reduced by approximately 2 cm/s thanks to the braking maneuver. Reducing the impact velocity has a huge effect on the bouncing. Indeed, lower impact velocity leads to greatly reducing the chances of bouncing off Dimorphos after impact, reducing the duration of bouncing and decreasing the number of bounces.

Future work

The research proposed in this thesis could be improved in several ways suggested below.

- The vectorized integrator was only tested to solve one initial value problem in parallel. However for the braking maneuver, the shape models and the bouncing, many integrations are made. It would thus be interesting to implement the vectorized integrator to carry out integration split several times.

- The braking maneuver implemented was a simpler implementation of the RCS system. The GNC could be implemented to perform the additional maneuvers during the descent and the final braking maneuver.

- The facet detection in shape models could be improved by using SPICE kernels to find efficiently which facet is crossed during the descent. This would improve the computational time of the current implemented method.

- The bouncing of the Monte Carlo analysis was performed on the smooth ellipsoid model. However, it could be interesting to carry out the analysis on an arbitrary shape model.
- A complex rock distribution algorithm could be implemented to model the rocks on the surface. For instance, adding rocks on a facet of the shape model and see the resulting interaction with the spacecraft.
- Juventas is considered as a point mass body. To represent the real shape of the CubeSat, Juventas could be modeled as a box. This would result in many more interesting interactions during the descent and the bouncing.

Appendix A

Inertial to synodic reference frame

At time t, the position $\boldsymbol{r}_{moon}$ and velocity $\boldsymbol{v}_{moon}$ of Dimorphos is computed in the inertial reference frame centered at the barycenter of the system using SPICE kernels. The matrix of transformation between the inertial and synodic reference frame is given by

$$\boldsymbol{X} = \frac{\boldsymbol{r}_{moon}}{\|\boldsymbol{r}_{moon}\|} \quad \boldsymbol{Z} = \frac{\boldsymbol{r}_{moon} \times \boldsymbol{v}_{moon}}{\|\boldsymbol{r}_{moon} \times \boldsymbol{v}_{moon}\|} \quad \boldsymbol{Y} = \boldsymbol{Z} \times \boldsymbol{X} \tag{A.1}$$

$$\boldsymbol{R}_{in \to syn}(t) = \begin{bmatrix} \boldsymbol{X} & \boldsymbol{Y} & \boldsymbol{Z} \end{bmatrix} \tag{A.2}$$

The position $\boldsymbol{r}_{syn}$ and velocity $\boldsymbol{v}_{syn}$ of the spacecraft in synodic frame is retrieved from the position $\boldsymbol{r}_{in}$ and velocity $\boldsymbol{v}_{in}$ in inertial frame. The transformation is given by

$$\boldsymbol{r}_{syn} = \boldsymbol{R}^{T}_{in \to syn}(t)\boldsymbol{r}_{in} \tag{A.3}$$

$$\boldsymbol{v}_{syn} = \boldsymbol{R}^{T}_{in \to syn}(t)\boldsymbol{v}_{in} - [0 \ 0 \ \omega] \times r_{syn} \tag{A.4}$$

where ω is the instantaneous angular velocity of the frame.

$$\omega = \left\| \frac{\boldsymbol{r}_{moon} \times \boldsymbol{v}_{moon}}{||\boldsymbol{r}_{moon}||^2} \right\| \tag{A.5}$$

Appendix B

Note on shape models

Each facet of the shape model is represented by a triangle as in Figure B.1. The only information about shape models are the position of the vertices. Let $\boldsymbol{P}_1, \boldsymbol{P}_2$ and $\boldsymbol{P}_3$ be three dimensional vectors representing the vertices. Let $\boldsymbol{a}, \boldsymbol{b}$ and $\boldsymbol{c}$ be three dimensional vectors representing the edges. Let $\boldsymbol{n}$ be the normal of the facet.

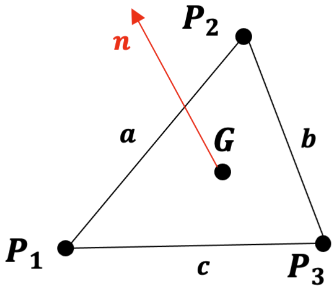

Figure B.1: Representation of a facet

The center of the facet is computed by :

$$\boldsymbol{G} = (\boldsymbol{P}_1 + \boldsymbol{P}_2 + \boldsymbol{P}_3)/3 \tag{B.1}$$

The edges are computed by :

$$\begin{aligned} \boldsymbol{a} &= \boldsymbol{P}_2 - \boldsymbol{P}_1 \\ \boldsymbol{b} &= \boldsymbol{P}_3 - \boldsymbol{P}_2 \\ \boldsymbol{c} &= \boldsymbol{P}_3 - \boldsymbol{P}_1 \end{aligned}$$

And finally, the normal of the facet is computed by :

$$\boldsymbol{n} = \frac{\boldsymbol{a} \times \boldsymbol{c}}{\|\boldsymbol{a} \times \boldsymbol{c}\|}$$

Appendix C

Results bouncing : $e = 0.1,\ f = 0.1$

Without braking maneuver		
Parameters	Mean value	1-σ value
Number of bounces	1.7860	0.4102
Height first bounce	0.54293 m	0.0542 m
Duration bouncing	5.6820 min	0.5100 min
With braking maneuver		
Parameters	Mean value	1-σ value
Number of bounces	1	0
Height first bounce	0.27266 m	0.0236 m
Duration bouncing	3.6540 min	0.1740 min

Table C.1: Summary bouncing for $e = 0.1,\ f = 0.1$

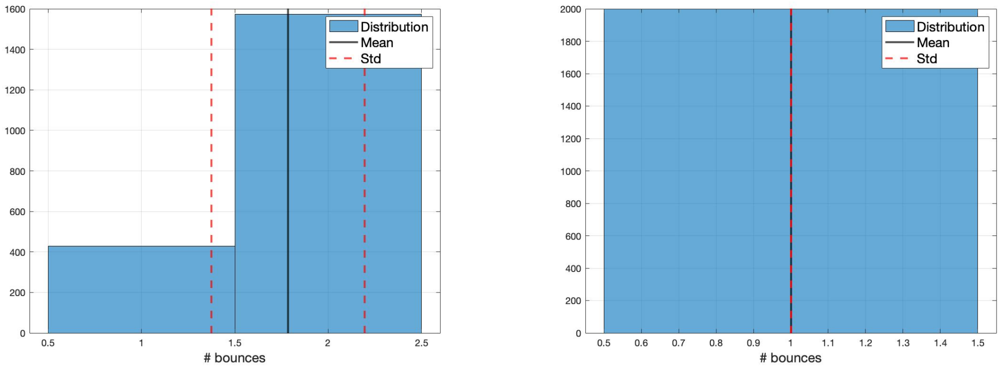

(a) Without braking maneuver

(b) With braking maneuver

Figure C.1: Histogram number of bounces for $e = 0.1,\ f = 0.1$

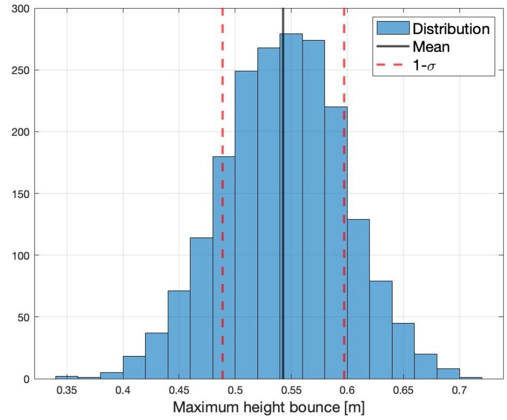

(a) Without braking maneuver

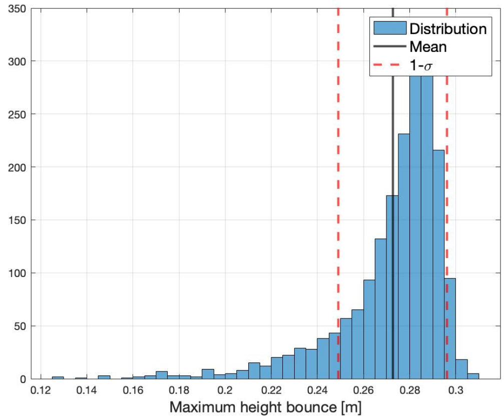

(b) With braking maneuver

Figure C.2: Histogram height of first bounce for $e = 0.1,\ f = 0.1$

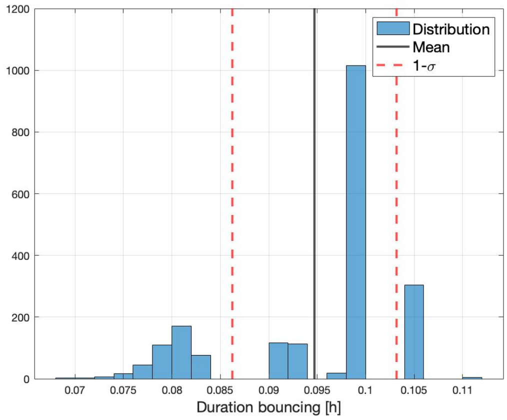

(a) Without braking maneuver

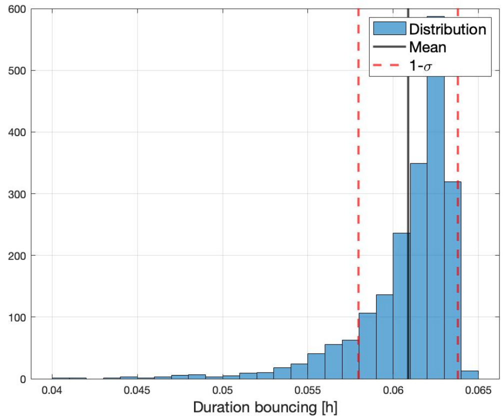

(b) With braking maneuver

Figure C.3: Histogram duration bouncing for $e = 0.1,\ f = 0.1$

Bibliography

[1] European Space Agency. *Didymos Reference Model V5.5*. 03. Mar. 2021.

[2] NASA/Naidu et al. *AIDA Workshop, 2016*. URL: https://www.nasa.gov/sites/default/files/thumbnails/image/screen_shot_2017-06-30_at_12.03.56_pm.png.

[3] Patrick Michel et. al. and Hera Science Team. "The ESA Hera mission to the binary asteroid (65803) Didymos: Planetary Defense and Science". In: *European Planetary Science Congress 2021* (2021). DOI: https://doi.org/10.5194/epsc2021-71.

[4] *Associated Legendre polynomials*. URL: https://en.wikipedia.org/wiki/Associated_Legendre_polynomials.

[5] Camilla Colombo. *Orbital Mechanics*. Chapter 6, orbital perturbations, course note class of Fall 2019.

[6] DART. *ADDDD*. URL: https://dart.jhuapl.edu/SOC/Data/Derived-Products/Simulated/Shape-Model/.

[7] Daniel D. DURDA et al. "Detecting crater ejecta-blanket boundaries and constraining source crater regions for boulder tracks and elongated secondary craters on Eros". In: *Meteoritics & Planetary Science* (2012). DOI: https://doi.org/10.1111/j.1945-5100.2012.01380.x.

[8] Shampine L. F. and M. W. Reichelt. "THE MATLAB ODE SUITE". In: *SIAM Journal on Scientific Computing* (1997). URL: https://www.mathworks.com/help/pdf_doc/otherdocs/ode_suite.pdf.

[9] Erwin Fehlberg. *Classical fifth-, sixth-, seventh-, and eighth-order Runge-Kutta formulas with stepsize control*. National Aeronautics and Space Administration, 1992.

[10] GMV. *Juventas GNC landing: landing mil simulation*. PowerPoint presentation.

[11] GMV. *Juventas Landing Workshop: Navigation during descent final approach*. PowerPoint presentation. 5-02-2021.

[12] et.al. H. Goldberg O. Karatekin. *Development of the juventas cubesat for hera icubesat 2019*. 2019. URL: https://icubesat.files.wordpress.com/2019/05/a.4.2.201905261444-goldberg.pdf.

[13] E. Hairer, S. P. Nørsett, and G. Wanner. *Solving Ordinary Differential Equations I : Nonstiff Problems*. Springer, 1992.

[14] Guillaume Hanon and Guillaume Vanhalst. "A study of the landing phase of the Juventas CubeSat on the moon of the binary asteroid system Didymos". MA thesis. École polytechnique de Louvain, 2020.

[15] Juventas CubeSat for Hera. "JUVENTAS MISSION ANALYSIS REPORT (MAR) V1.4". In: *JUV-GS-MAR-001* (2019).

[16] *Impactor Spacecraft*. 2021 The Johns Hopkins University Applied Physics Laboratory. URL: https://dart.jhuapl.edu/Mission/Impactor-Spacecraft.php.

[17] Ozgur Karatekin. *Landing Workshop 2 : Science goals & summary of 1st landing workshop*. Royal Observatory of Belgium. 2021.

[18] Kaula W. M. *Theory of Satellite Geodesy: Applications of Satellites to Geodesy*. Dover edition, 2000.

[19] Yoshikawa M. et al. "The nature of asteroid Itokawa revealed by Hayabusa". In: *Near Earth Objects, our Celestial Neighbors: Opportunity and Risk* (2006). DOI: https://doi.org/10.1017/S174392130700350X.

[20] MathWorks. *Vectorization*. URL: https://www.mathworks.com/help/matlab/matlab_prog/vectorization.html.

[21] Mathworks. *ODE Event Location*. URL: https://www.mathworks.com/help/matlab/math/ode-event-location.html.

[22] Patrick Michel, Michael Küppers, and Ian Carnelli. "The Hera mission: European component of the ESA-NASA AIDA mission to a binary asteroid". In: *Lunar and Planetary Science Conference 2018* (2018). DOI: https://doi.org/10.1016/j.asr.2017.12.020.

[23] *Mission Overview*. 2021 The Johns Hopkins University Applied Physics Laboratory. URL: https://dart.jhuapl.edu/Mission/index.php.

[24] Gaskell R. et al. *Gaskell Itokawa Shape Model V1.0*. URL: https://ui.adsabs.harvard.edu/abs/2008PDSS...92.....G/abstract.

[25] Hanspeter Schaub and John L. Junkins. *ANALYTICAL MECHANICS of AEROSPACE SYSTEMS*. AIAA EDUCATION Series, 2002.

[26] Daniel J. Scheeres. *Orbital Motion in Strongly Perturbed Environments : Applications to Asteroid, Comet and Planetary Satellite Orbiters*. Springer, 2012.

[27] Simon Tardivel and Daniel J. Scheeres. “Contact Motion on Surface of Asteroid”. In: *JOURNAL OF SPACECRAFT AND ROCKETS* (2014). DOI: 10.2514/1.A32939.

[28] Simon Charles Vincent Tardivel. “The Deployment of Scientific Packages to Asteroid Surfaces”. PhD thesis. University of Colorado, 2014.

[29] Juventas Team. *JUV-GNC-GMV-MEMO-0003*. GMV.

[30] *The Juventas CubeSat in Support of ESA’s Hera Mission to the Asteroid Didymos*. 33rd Annual AIAA/USU Conference on Small Satellites. 2019. URL: https://digitalcommons.usu.edu/cgi/viewcontent.cgi?article=4372&context=smallsat.

[31] *The Mission*. URL: https://www.heramission.space/mission.

[32] Eric W. From MathWorld–A Wolfram Web Resource Weisstein. *Legendre polynomial*. URL: https://mathworld.wolfram.com/LegendrePolynomial.html.

[33] Hajime Yano et al. “Touchdown of the Hayabusa Spacecraft at the Muses Sea on Itokawa”. In: *SCIENCE* 312 (2006). DOI: https://doi.org/10.1126/science.1126164.

UNIVERSITÉ CATHOLIQUE DE LOUVAIN
École polytechnique de Louvain
Rue Archimède, 1 bte L6.11.01, 1348 Louvain-la-Neuve, Belgique | **www.uclouvain.be/epl**